Science of the Total Environment 946 (2024) 174283

Contents lists available at ScienceDirect

Science of the Total Environment

journal homepage: www.elsevier.com/locate/scitotenv

Utilization of abandoned oil well logs and seismic data for modeling and assessing deep geothermal energy resources: A case study

Ahmed Shawky [a,b,*], Mohamed Ibrahim El-Anbaawy [b], Reham Soliman [c], Eslam Nasr Shaheen [d], Osama Abdelaziz Osman [e], Hesham Eid Abdel Hafiez [f], Nahla Ahmed Shallaly [b]

[a] Department of Energy and Fluid Mechanics, School of Industrial Engineering (EII), University of Valladolid (UVa), Valladolid, Spain
[b] Geology Department, Faculty of Science, Cairo University, Giza, Egypt
[c] Environmental Engineering Program, Zewail City of Science and Technology, 6th of October City, Giza, Egypt
[d] Seashell Energy Services Co. Ltd, Cairo, Egypt
[e] Qarun Petroleum Company, New Maadi, Cairo, Egypt
[f] National Research Institute of Astronomy and Geophysics (NRIAG), Helwan, Cairo, Egypt

HIGHLIGHTS

- Seismic data and well logs from abandoned oil wells were utilized for geothermal energy exploration and assessment.
- A Complete geologic picture of Hammam Faraun geothermal system and a conceptual model were constructed.
- A magma chamber exists at a depth of 20-30 km beneath Hammam Faraun area and plays a main role in its geothermal system.
- Monte Carlo simulations revealed a promising geothermal power potential of Hammam Faraun area (9.64 MWe to 43.76 MWe)
- From 12000 to 53000 households in Sinai could be supplied with clean electricity from a geothermal power plant in the area.

GRAPHICAL ABSTRACT

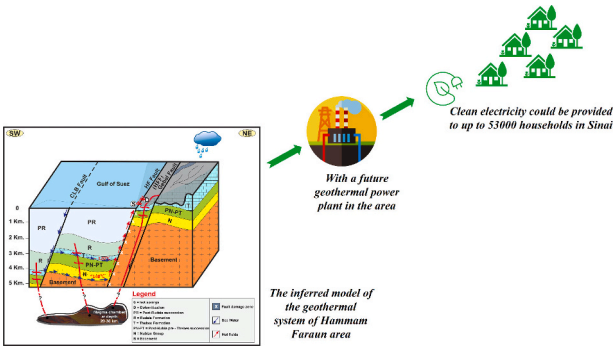

ARTICLE INFO

Editor: Jose Julio Ortega-Calvo

Keywords:
Geothermal energy
Rift
Hammam Faraun (HF)
Geomechanical model
Dilation tendency
Magma chamber
Monte Carlo simulation

ABSTRACT

Hammam Faraun (HF) geothermal site in Egypt shows potential for addressing energy demand and fossil fuel shortages. This study utilizes abandoned oil well logs, seismic data, and surface geology to assess HF geothermal energy resources.

Seismic interpretation identified a significant clysmic fault parallel to Hammam Faraun fault (HFF), named CLB fault. The two faults together create a renewable geothermal cycle through circulation of mixed formation-sea waters.

Petrophysics revealed two main geothermal reservoirs: the Nubian sandstone reservoir and the Eocene Thebes carbonate reservoir with water saturation values approaching 100 %. Corrected borehole temperatures indicated reservoir temperatures around 120 °C and 140 °C for the Thebes and Nubian reservoirs, respectively.

* Corresponding author at: Department of Energy and Fluid Mechanics, School of Industrial Engineering (EII), University of Valladolid (UVa), Valladolid, Spain.
E-mail addresses: ashawkym@sci.cu.edu.eg, ahmedshawky.mohamed@uva.es (A. Shawky).

https://doi.org/10.1016/j.scitotenv.2024.174283
Received 19 December 2023; Received in revised form 21 June 2024; Accepted 23 June 2024
Available online 27 June 2024

Fracture analysis and stress state provided insights into subsurface fractures. A geomechanical model demonstrated the impact of different stresses and pore pressure on geothermal fluid flow. NE-SW oriented fractures showed a higher dilation tendency due to aquathermal expansion.

The integrated conceptual geothermal model suggested a magma chamber beneath HF as the heat source, related to Oligo-Miocene volcanic activity. The breached relay ramp and fault-related open fracture system serve as pathways for geothermal fluids.

Evaluation of the geothermal potential utilized volumetric calculations and Monte Carlo simulation. The estimated hot water volumes were 1.72 km^3, 4.242 km^3, and 5.332 km^3 for the Nubian reservoir in the onshore part, Thebes reservoir in the offshore part, and Nubian reservoir in the offshore part, respectively.

The results indicate a medium enthalpy resource suitable for electricity generation using a Kalina geothermal power plant. The predicted geothermal power output is promising, with an average power output of 9.64 MWe, 21.38 MWe, and 43.76 MWe for the Nubian reservoir in the onshore part, Thebes reservoir in the offshore part, and Nubian reservoir in the offshore part, respectively. These outputs can potentially supply electricity to approximately 12,000, 29,000 and 53,000 households, respectively.

1. Introduction

By 2050, energy demand could double or triple due to population growth and developing nation economic growth (Glassley, 2015). Due to global and national energy shortages and climate change, new and environmentally friendly energy sources are needed to overcome these issues. Thus, energy generation from renewable sources is becoming increasingly essential (Fatona, 2011). Access to clean, affordable energy improves living standards of developing nations (Fridleifsson, 2001). By 2100, renewable energy might supply 80 % of total energy consumption (Fridleifsson, 2001, 2013). Geothermal energy is such a viable renewable energy source.

Geothermal energy is the natural heat obtained from Earth's subsurface. Hot water and/or steam transports this energy to the surface. Geothermal energy can be harnessed for clean electricity generation, heating, and cooling (IRENA, 2017). Due to its higher capacity factor than other renewable sources, geothermal power may provide baseload electricity and auxiliary services for short- and long-term flexibility. Geothermal power sources emit significantly less greenhouse gases than fossil fuels (Goldstein et al., 2011).

With the rising energy demand for sustainable development in Egypt, the government has prioritized renewable energy sources in the last decade, establishing some mega-scale projects, particularly in solar and wind energies. However, one other source that has not gained the required attention is geothermal energy. Hammam Faraun (which means Pharaoh's bath) is an area that lies in the western part of the Sinai Peninsula in Egypt, i.e., on the eastern shore of the Gulf of Suez (GOS) rift (Fig. 1a). The area is well known for a strip of hot springs running parallel to the shoreline with a surface temperature of 70 °C, forming a longitudinal lake facing the well-known geomorphologic high called Gebel (mountain) Hammam Faraun (Figs. 1b, c, d, e). Two karstic caves are found at the foot of Gebel Hammam Faraun (Figs. 1f, g), where hot springs also emerge from deep inside. The area is an important destination of balneotherapy, inside-cave sauna and geologic field trips (Shawky et al., 2020).

HF area is distinguished by an elevated geothermal gradient and high heat flow, with estimated geothermal gradient values reaching 48 °C/km and heat flow values reaching 120 mW/m^2 (Boulos, 1989; Morgan et al., 1985; Abdel Zaher et al., 2012; Lashin, 2013). A large hot spot occurs beneath and to the southwest of the area (Alsharhan, 2003).

HF was one important area selected by some researchers for geothermal studies in the GOS and Sinai (e.g., El-Qady et al., 2000; Atya et al., 2010; Abdel Zaher et al., 2011a;). Previous geophysical surveys include gravity, magnetic, magnetotelluric, and geoelectric resistivity. Analytic signal magnetic anomaly maps showed a maximum above HF hot springs, and geophysical processing showed 1.7 km depth to geothermal sources (Abdel Zaher et al., 2010). A high positive gravity anomaly was detected over the hot springs (Abdel Zaher et al., 2011b). Magnetotelluric studies (Abdel Zaher et al., 2011b) revealed a conductive region where resistivity increased with depth. Conductive zones were linked to the existence of a geothermal reservoir. On the other hand, a shallow body of high resistivity (<1 km) was found below HF hot springs, interpreted as the basement uplift in the heat source area. The 100-m-thick geothermal reservoir was defined by resistivity surveys (El-Qady et al., 2000). However, Abdel Zaher et al. (2012) assumed 500 m reservoir thickness. However, deeper, and more accurate geologic and geophysical data from seismic and well logs of abandoned oil wells in the offshore area of HF are utilized in this paper to better assess its deep geothermal energy resources.

Geological and geophysical methods are used to evaluate geothermal resources, including reservoir geometry, water capacity, and energy capacity. Thus, seismic data combined with wireline log data can be one of the best tools in geothermal exploration.

Petrophysics can be efficiently used for studying geothermal systems. The identification and characterization of geothermal reservoirs relies greatly on some petrophysical parameters which are necessary for geothermal system modeling. Thus, petrophysical approaches have made important progress in this field (Frolova et al., 2001; Clennell et al., 2010).

Recently, geomechanics has gained an obvious interest for geoscientists and engineers in both petroleum and geothermal industries, as well as for researchers interested in stress measurements and their application to faulting and fluid flow (e.g., Zoback, 2007). Fluid transport and migration depend on fractures and faults which control magma and geothermal fluid distribution. Fluid existence and migration in fault and fracture systems affect stress, mechanical failure, and chemical properties. However, not all faults and fractures in such systems contribute to fluid migration. This depends on their spatial distribution and orientation relative to the in-situ stress field and fluid pressure. Therefore, some faults can slip while others remain stable. Critically stressed frictional failure or near-failure faults act as effective conduits for fluids. Thus, fault stress can measure permeability at a scale of hundreds of meters (Hubbert and Rubey, 1959; Sibson, 1977; Barton et al., 1995; Morris et al., 1996; Sibson, 1996; Tezuka and Niitsuma, 2000; Townend and Zoback, 2000; Moeck et al., 2009; Faulkner et al., 2010; Siler et al., 2015; Giambiagi et al., 2019).

Geochemical analysis of rocks in geothermal areas reveals reservoir characteristics, heat source origins, fluid-rock interactions, and geothermal system changes. Therefore, this work uses a multiapproach combining seismic, petrophysical, geomechanical, and geochemical techniques for better understanding of the geothermal reservoirs in the study area. This paper aims to assess and model the geothermal energy system underneath Hammam Faraun and reduce the uncertainty in estimates of the geothermal resources of HF area. Four main issues regarding geothermal energy in HF area are addressed: possible geothermal reservoirs, geothermal fluid flow mechanism and how is it impacted, possible heat sources, and the temperatures, volumes, and potential uses of hot water in the reservoirs.

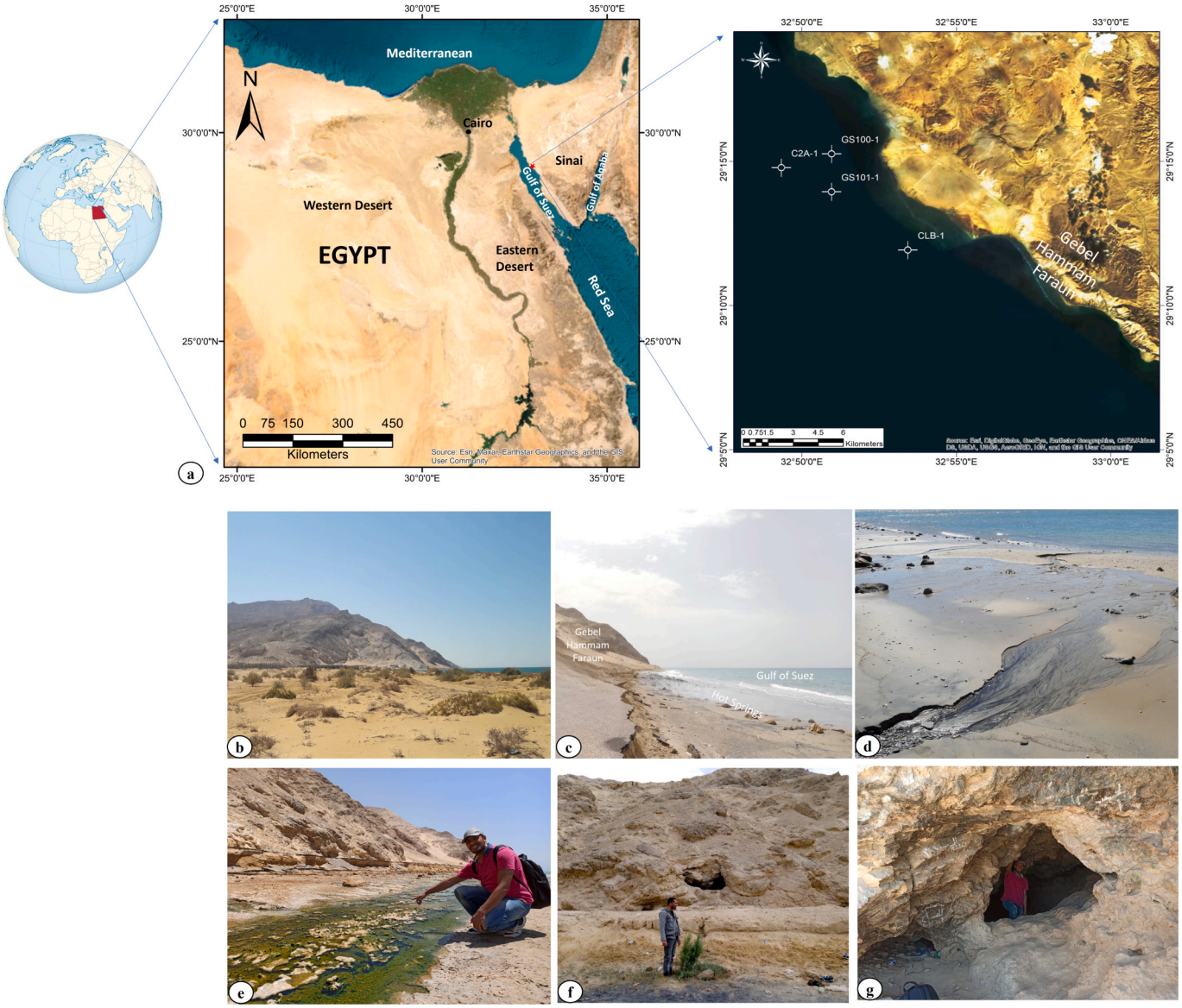

Fig. 1. Location maps and field photos of Hammam Faraun area, Sinai, Egypt. a) Satellite images showing the location of the area and the exact location of the four abandoned offshore oil wells used in the study. b) Far-reaching view of Gebel Hammam Faraun high, directly facing the Gulf of Suez with a narrow coast in between. c) the hot springs (70 °C) forming a strip along Hammam Faraun Fault (HFF) which is parallel to the shoreline. d) a fan-like pattern formed by the hot springs discharging into the Gulf of Suez e) green, yellow, and orange colors inside lakes formed by the hot springs caused by the presence of certain microorganisms, specifically thermophiles. f, g) the big karstic caves formed inside Gebel Hammam Faraun.

Rift basin geothermal energy exploration, especially in Africa, has yielded promising results. Kenya leads in geothermal power plants in the East African Rift System (EARS). Plans are underway to expand geothermal energy facilities in the EARS, which could generate 15,000 MW (Kombe and Muguthu, 2019; Elbarbary et al., 2022). Thus, the EARS shows the successful use of integrated geoscience methods, with plans to further geothermal exploitation. Geothermal energy project planning requires knowledge of rift basin geology. This work emphasizes on the GOS rift being an extension of the great EARS.

2. Geologic setting

The research area encompasses the north-western section of the Hammam Faraun rift block in the GOS rift. This intracontinental rift is characterized by thinned crust, rift-related volcanic activity, and elevated heat flow, making it an ideal setting for a geothermal play system (Shawky et al., 2021 and references therein). The HF geothermal system can be categorized under both fault-controlled, extensional, convection-dominated and magmatic, convection-dominated geothermal play types according to the catalog of Moeck (2014). The hot springs of the HF area are located along the so-called Hammam Faraun Fault (HFF). HFF is a major rift-related significant fault associated with the eastern margin of the GOS rift. It spans over 25 km in length, with a steep southwest dip (60–80°) and a remarkable displacement of up to 5 km (Fig. 2).

The footwall occurs at the onshore part of the area while the hanging wall falls in the GOS. A nearly 500 m wide damage zone containing fracture corridors and significant brecciation characterize HFF. The fault exhibits a distinctive zigzag pattern in the map view, the major fault segment strike is NW-SE, with subordinate N-S, NNE-SSW, and WNW-ESE fault segments. The area is affected mainly by extension tectonic regime related to the GOS rifting and includes faults, fault-related folds, and fracture corridors (Moustafa and Abdeen, 1992; Sharp et al., 2000; Jackson et al., 2002; Gawthorpe et al., 2003; Jackson et al., 2006;

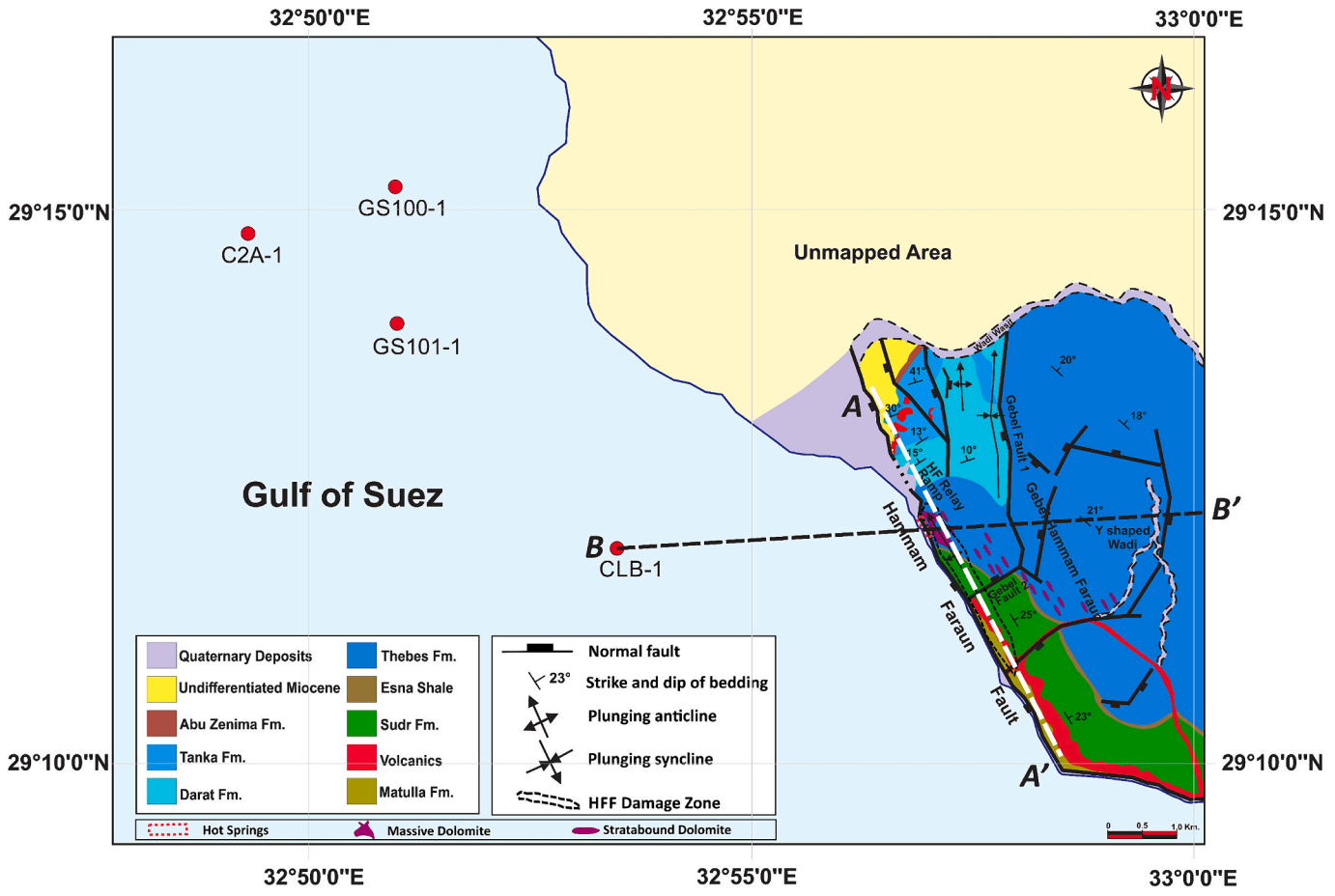

Fig. 2. A geologic map of HF area illustrating surface rock units, structural elements, the four offshore oil wells used in the study, and the traces of the two constructed cross sections (A A' and B B').

Rotevatn and Bastesen, 2014; Korneva et al., 2018; Shawky et al., 2021). A breached relay ramp occurs in the northwestern part of the area (Fig. 2) and is referred to as HF relay ramp (Shawky et al., 2021).

The HF rift block stratigraphy, comprising the HF area (Fig. 2), is divided into three sequences: pre-rift, *syn*-rift, and post-rift. From bottom to top, the pre-rift (pre-Oligocene) sequence consists of a sandstone assemblage, a mixed facies assemblage, and a carbonate assemblage. The pre-rift sequence is then overlain by an Oligocene-Miocene syn-rift phase that comprises early rift volcanics as well as clastics and evaporites. Following the two series is a post-rift (quaternary) sequence consisting of alluvium and wadi deposits. (e.g., Moustafa and Abdeen, 1992; Moustafa and Khalil, 2017). The visible surface rock units in the study area range in age from Senonian (namely Matulla Fm.) to quaternary (e.g., Moustafa and Abdeen, 1992; Hollis et al., 2017; Shawky et al., 2021). The hot springs issue from the fractured, partially dolomitized, and karstified Early Eocene (Ypresian) limestone of the Thebes Fm. (El Ramly, 1969; Magaritz and Issar, 1973; Swanberg et al., 1983; Hollis et al., 2017; Shawky et al., 2021).

The hydrothermal dolomitization phenomenon of the Thebes limestone in HF area gained special attention from some authors with different interpretations for the source of the dolomitizing fluids and the fluid circulation mechanism. These studies revealed that the dolomitizing fluids are either from hot brines or seawater mixed with formational waters that circulated along the fault system, resulting in different generations of dolomites. Two modes of dolomitization were inferred, namely, massive dolomite and strata-bound dolomite with different geometries, petrographic properties, and origins (Magaritz and Issar, 1973; Hirani, 2014; Hollis et al., 2017; Korneva et al., 2018; Hirani et al., 2018a, 2018b). A recent model for the sequential development of hydrothermal deposits along the rift-related HFF has been introduced by Shawky et al. (2021) who also made a first-time documentation of HF travertine deposits and draw attention to HF karstic features. This model suggests that, at rift commencement, strata-bounded dolomite represented the hydrothermal deposits associated with fluid circulation, but at rift climax, massive dolostone was formed from mixed water from coastal lakes. These dolomitizing lakes filled the topographically low region on the HF relay ramp's flank. Travertine deposits formed later, with the commencement of post-rifting time, from fluids inside spring lakes during the Pleistocene pluvial period. This suggests that geothermal activity has been ongoing since the rift's commencement to the present.

The rift-related volcanic rocks in the HF area form a fault-bounded NW-inclined sheet flow, sills, and dykes. The conspicuous dyke-sill complex intrudes the pre-rift sequence. Basaltic flows and sills were recorded in the northwestern part of the study area (HF relay ramp). In contrast, the southeastern part is occupied by two dykes forming a ring dyke and a sill (Fig. 2). Petrographically, the dykes and sill margins are composed of amygdaloidal glassy olivine-augite-plagioclase-phyric basalt. Small enclaves of plagioclase vitrophyric basalts are recorded in this variety, implying the presence of more than one generation of basalts. On the other hand, medium-grained olivine-dolerite fills the interior of the sill and the dykes (Shawky et al., 2021; Shallaly et al., 2023). These basaltic intrusions have a K—Ar age of 22–24 Ma (Steen, 1982). Therefore, denoting the early stage of rifting.

The interplay of sedimentation and rift-related volcanism in HF area developed skarn rocks (Abdel Kader and El Aref, 1986; Shallaly et al., 2023) and peperites (Shallaly et al., 2023). Skarns were documented along the contacts of the basaltic sill and the pre-rift Late Cretaceous

Sudr Chalk, while peperites were recognized along the contacts between the Early Miocene Nukhul Fm. and the basaltic sills. Basaltic intrusions induced marbelization of several host carbonate rocks (Shallaly et al., 2023).

3. Materials and methods

Application of different field, office, and laboratory techniques was carried out to achieve the aim of the study. The data used included well logs for four offshore wells and twenty seismic lines obtained from the Egyptian General Petroleum Corporation (EGPC) and Gulf of Suez Petroleum Company (GUPCO). The four wells are CLB-1, GS 101–1, GS 100–1, and C2A-1 in order of proximity to the hot springs area. The seismic lines are 2D lines in the depth domain. These data are not publicly available and can be only accessed through submission of a request to the EGPC or to the Egypt Upstream Gateway "EUG" (EUG, 2021) to be used for academic research purposes.

Stratigraphic and composite well logs were used in the lithological description of the subsurface rock units. Moreover, the well log data of the four wells have been utilized in stratigraphic correlations between subsurface formations. These correlations are performed using essentially the traditional wireline logs and are based on visual pattern recognition and sequence matching using electric log markers and selecting characteristic log responses.

Due to the low quality of the seismic data in some parts of the area and the missing of some parts due to the existence of the area of interest on the margin of the seismic survey, problem-solving cross sections were constructed. They were constructed using surface geology as well as formations tops and dipmeter data (formation dips) from the available well data.

The seismic interpretation was performed using Petrel software (SLB, 2024a). It was covered in several steps, starting with reflector identification, picking, and correlating reflectors, picking horizons and fault locations, and eventually the construction of geo-seismic cross-sections. Seismic interpretation aimed to delineate subsurface strata, determine the geometry of the geothermal system, and construct structural depth maps that were used later for volumetric analysis.

A petrophysical analysis was carried out to reveal and characterize the possible geothermal reservoirs. To assess the petrophysical properties of the main lithological units, borehole geophysical logs of the four wells in the offshore part of the study area were used. The log analysis software Schlumberger Techlog (SLB, 2024b) was used to perform this complex integrative operation.

Structural measurements for fracture sets in the field were carried out using a Brunton compass and the "Fieldmove Clino" smartphone application (Petroleum Experts Limited, 2024). The goal of these measurements was to identify different fractured zones and their possible extension and penetration, as well as their geothermal significance. Data recorded for the fracture sets included fracture type, orientation, intensity, type of cement fill, and spatial and dimensional characterizations. This was followed by the construction of 1D geomechanical model (mechanical earth model; MEM) using Techlog software (SLB, 2024b).

Volcanic rock samples from the studied area and its environs were collected in the field for geochemical analysis to detect their source and their significance on the geothermal system. A total of seventeen samples were powdered and analyzed for major and trace element composition using the X-ray fluorescence (XRF) technique at the laboratories of Erlangen University, Germany, and the central laboratories of the Egyptian Mineral Resources Authority (EMRA). XRF is a well-known, established, and commonly used technique for determining the main elemental compositions of earth materials. It allows for the non-destructive analysis of solid samples using X-radiation (e.g., Oyedotun, 2018).

The temperature logs obtained immediately after drilling operations may provide the sole temperature data available from deep wells. Nevertheless, these readings are still subject to the thermal disruption induced by drilling and hence do not accurately reflect the actual temperatures of the reservoir. This thermal disturbance is contingent upon various elements, including drilling duration, logging methodology, and mud temperature. Geothermal projects rely on precise thermal data, and temperature correction provides an opportunity to determine whether these fields are suitable for geothermal energy extraction (Schumacher and Moeck, 2020). Therefore, it is essential to correct the borehole temperatures before utilizing them in geothermal resource assessment. Correction methods used are Waples et al. (2004) and the simple method designed by ZetaWare (2003). Due to the limited availability of time since circulation (TSC) data in the wells under study, temperature corrections are only applied to a few bottom hole temperatures. The method described by Waples et al. (2004) involves the use of the following equation:

$$T_{true} = T_{surf} + f\left(T_{meas} - T_{surf}\right) - 0.001391 \bullet (Z - 4498) \quad (1)$$

where T_{meas} is the measured log temperature in Celsius, Z is depth below sea floor in meters and T_{surf} is the sea floor or land surface temperature. The correction factor, f, is a function of TSC and is calculated using the following equation:

$$f = 1.32866^{-0.005289 \cdot TSC} \quad (2)$$

where TSC is the time since circulation in hours. The geothermal gradient GG was calculated using the following equation:

$$GG = (BHT - MST)/Z \quad (3)$$

where BHT is the bottom hole temperature, MST is the mean annual surface temperature assumed to be 26.7 °C (Boulos, 1990), and Z is the depth at which the corresponding temperature is recorded.

Surface and subsurface data were integrated to construct a final geothermal conceptual model.

Eventually, volumetric calculations to determine the volume of the water in the geothermal reservoirs using software map-based calculations were performed and the resulting volumetrics were used together with other reservoir parameters to access the energy capacity of the HF geothermal system. Volumetric calculations in Petrel allow to accurately calculate fluid volumes in a 3D grid using properties, constants, contacts, and recovery factors as inputs. These calculations are essential for evaluating the economics of a project and understanding the possible range of hydrocarbon volumes in an exploration lead or prospect. However, in this paper we have used this method to calculate the volume of water in the geothermal reservoirs. First, the top surface and the base surface of each reservoir is defined fluid contacts were identified and defined, the most important was the oil-water contact (OWC). This contact represents the boundary between the water and hydrocarbon zones (if any). Secondly, volume calculations were performed using the map-based volume calculation module to calculate the volume of water in the reservoir. The module allows the user to input petrophysical parameters, maps, and contacts to obtain accurate volume estimates.

The main equation used in this method can be written as following:

Volume of water in a reservoir:

$$V = A \cdot h_v \cdot \phi \cdot S_w \quad (4)$$

where A, area (average); h_v, net thickness = $h \cdot NTG$; ϕ, porosity; S_w, water saturation; and NTG, net to gross. The net-to-gross ratio (NTG) represents the proportion of the bulk volume of a reservoir that contains reservoir-quality rock or fluids. It takes into account the presence of non-reservoir rocks, such as shale or non-porous formations, within the reservoir interval. The volume of oil is ignored here as the studied wells show nearly 100 % water saturation.

The volumetric method is applied to assess the volume of the geothermal water due to its straightforwardness and convenience. Monte Carlo simulation approach was adopted in parallel with the application of volumetric approach estimating the potential geothermal

resources of Hammam Faraun area. The triangular distribution model was adopted in this study which is defined by three points—the minimum, most likely, and maximum values. This simulation was accomplished using Python-based Monte Carlo simulation following the method developed by Pocasangre and Fujimitsu (2018) and recently applied by Elmasry et al. (2023) in assessing the geothermal power potential in the Northern part of Egypt. Monte Carlo simulation using Python code is applied to model the uncertainties associated with various parameters involved in power generation and the estimation of power generation through random sampling, it was set to generate 1000 samples for each variable input. Two scenarios were applied, 25-year and 50-year power plant lifetimes. The following equations are used:

For the calculation of the available thermal energy stored in rocks and water:

$$Q_r = A{\cdot}h{\cdot}\rho_r{\cdot}C_r \bullet (1-\phi) \bullet (T_r - T_s) \tag{5}$$

$$Q_w = A \bullet h_v{\cdot}\rho_w \bullet C_w \bullet \phi \bullet (T_r - T_s) \tag{6}$$

$$Q_T = Q_r + Q_w \tag{7}$$

where Q_r and Q_w are thermal energy reserved in rock and in the pore water, respectively, Q_T is the total stored thermal energy in the rock (KJ), A represents the area of the thermal reservoir, h represents the thickness of the reservoir (m), h_v is the net reservoir thickness, ρ_r and ρ_w are the rock density and water density (kg/m^3), respectively, C_r and C_w are the rock specific heat and water specific heat (kJ/kg-°C), respectively, ϕ is rock porosity (%), T_r and T_s are the average temperatures of reservoir and surface, respectively (°C).

The heat value is then multiplied by a coefficient known as the recovery factor to estimate the amount of usable heat that can be retrieved from the specified volume of reservoir. The recoverable heat energy, Q_R, can be calculated by multiplying the geothermal recovery factor, R_f, with the total heat of the geothermal resource as following:

$$Q_R = Q_T \bullet R_f \tag{8}$$

Finally, to estimate the technical potential for electrical power generation (Mwe), the following equation is used:

$$\dot{W} = Q_R \bullet \eta_T / F_c \bullet P_l \tag{9}$$

where η_T is the thermal energy efficiency of transformation, F_c is the capacity factor of the power plant, and P_l is the running period of the power plant.

4. Results and discussion

4.1. Subsurface geology

4.1.1. Subsurface stratigraphy

A succession related to the surface section in the HF area is encountered in the subsurface (the downthrown of the HFF). This section is studied in detail from the four offshore wells nearby to the study area, as mentioned previously. In addition to older rocks that were not recorded on the surface due to erosion, the encountered rock units are compiled and fully described in Table 1 in supplementary file. The lithological description of the two potential reservoirs (Thebes carbonate and Nubian sandstone) is given in Table 1.

4.1.2. Subsurface correlation

The process of subsurface correlation is useful in identifying the missing sections, stratigraphic thinning, lateral facies change, and unconformities. Furthermore, it enables estimating the number of missing sections and the depth of possible faults in the hanging wall of HFF to be taken into consideration in the final integrated model. Therefore, a well-log correlation panel for the subsurface stratigraphic units in the study area was constructed and shown in Fig. 1 in supplementary file.

4.1.3. Problem-solving cross-sections

The first geologic cross section is NW-SE oriented and shows the surface outcrops in the study area and the inferred subsurface units (Fig. 2a in supplementary file). The second one is ENE-WSW oriented (Fig. 2b in supplementary file). The latter displays the surface and subsurface stratigraphy and clearly shows the existence of a normal fault parallel to HFF and throwing toward SW. This fault is referred here to as CLB fault (or CLB-1 fault) as it cuts the CLB-1 well. CLB fault seems to play an important role in the circulation of geothermal fluids in HF geothermal systems together with HFF as both faults are parallel and cut both potential geothermal reservoirs. The second cross section integrates the geology of the hanging wall (representing the subsurface) and the footwall (representing the surface) of HFF. These cross sections have helped to solve structural problems and complete the geologic picture.

4.1.4. Seismic interpretation

The seismic interpretation reflects the outstanding role of faulting and folding on the different formations in the study area. The structural architecture of the study area is achieved through detailed seismic interpretation of dip and strike seismic profiles of important structural events and consequently construction of the detailed subsurface structural maps on the different picked horizons. The picked horizons include top Nubia A, top Thebes, Top Rudeis, and top Zeit. The first two horizons are selected where they are predicted to be the main geothermal reservoirs in the study area whereas the last two ones are selected to complete the subsurface structural architecture of the area.

The structural analysis of the interpreted NE-SW and NW-SE seismic profiles declares the structural style of the unexposed hanging wall of the HFF. The seismic profile passing through the studies well shows the occurrence of hangingwall faults in the hangingwall of the HFF in the subsurface (Fig. 3 in supplementary file). One important fault of these faults is the CLB fault penetrated by the CLB-1 well. Another seismic

Table 1
stratigraphic description of the potential geothermal reservoirs units encountered in the four studied wells.

Rock unit		Age	Thickness in wells	Lithological description
Thebes Fm.		Eocene	269 ft. (82 m) in CLB-1 well and a maximum thickness of 161 m in GS 101–1 well	Carbonate-dominated rocks; the lower part is dark brown to brownish grey, cryptocrystalline to finely crystalline, bituminous in part, and rarely glauconitic; overlain by white chalky cryptocrystalline limestone with chert bands; brown crystalline dolomite layers with occasion chert band and nodules are recognized within the limestone. Missed out on C2A-1 well.
Nubian Sandstone	Nubia-A	Late Paleozoic to Early Cretaceous	Not completely penetrated- the total drilled thickness reaches a maximum of 655 ft. (199.6 m) in GS101–1 well and a minimum of 138 ft. (42 m) in C2A-1 well	Intercalations of sandstone and shale with the shale dominating upward; sandstone is medium to fine-grained, whitish, subangular to subrounded, moderately sorted with calcareous to siliceous cement and glauconitic in part; shale is greenish grey to dark brown, sub-blocky to sub-flaky, non-calcareous, and occasionally silty
	Nubia-B	Paleozoic		Shale, siltstone, and claystone with sandstone intercalations llies on the basement rocks

profile passing through the GS 101–1 well shows the extension of the CLB fault in the northwest direction. Moreover, the seismic profile passing through the GS100–1 well shows another fault considered as a branch from the master fault of the Hammam Faraun fault. The branching of faults near accommodation zones is a common structural feature of rifts.

Structural depth maps are constructed for the tops of Nubia and Thebes formations (Fig. 4 in supplementary file). The maps illustrate the subsurface structural architecture of the study area in coincidence with the seismic cross sections. The hanging wall cut-offline of HFF is shown in the eastern parts of the maps. HFF is characterized by its bifurcation near the accommodation zone (Fig. 4 in supplementary file). One of these branches is that branch that occurs at the NE part of the seismically mapped area. The CLB fault to the SW of HFF which is another NW oriented fault throwing to the SW is also shown on these maps. A series of antiforms and synforms in the hanging wall of the CLB fault as well as the hanging wall of HFF (footwall of CLB fault) were formed due to the variation of fault throws along the strike of these faults. These antiforms and synforms are obvious on the structural depth maps.

4.2. Petrophysical investigation

The evaluated petrophysical properties are formation temperature, porosity (total and effective), formation water resistivity, and saturation (oil saturation and water saturation).

The following workflow for petrophysical characterization is followed:

a) Estimation of formation temperature.
b) Porosity models
c) Determination of formation water resistivity
d) Determination of water saturation and hydrocarbon saturation

The calculated petrophysical parameters from the well logs are combined altogether to construct the computer-processed interpretation (CPI) plots for two wells (GS100–1 and GS101–1) for which the quality of data was good enough to carry out petrophysical analysis (Fig. 3). The two water-bearing formations Nubia and Thebes are cropped and presented here.

GS 100-1 well

The CPI plot of Nubia Fm. in GS 100–1 well shown in (Fig. 3a) is well marked by a low resistivity curve where resistivity doesn't exceed 4.1. ohm*m. The average effective porosity is 21 %. The calculated average water saturation is near 98 % which is confirmed by the low resistivity curve. Likewise, the CPI plot of the Thebes Fm. (Fig. 3b) shows a moderate resistivity curve which is nearly 44.2 Ω*m. The average effective porosity is 10.7 % and the average water saturation is 99 %.

GS 101-1 well

The CPI plot of the Nubia Fm. (Fig. 3c) is characterized by a low to moderate resistivity curve where resistivity values range between 0.36 and 55.8 Ω*m. Average porosity and average water saturation are 16 % and 93 % respectively. For the Thebes Fm., the CPI plot (Fig. 3d) demonstrates moderate resistivity that doesn't exceed 35.4 Ω*m with average porosity equals to 15.7 % and 66.3 % average water saturation.

It can be concluded that the CPI plots show very low resistivity in the two water-bearing zones (Nubia and Thebes reservoirs) which supports the idea of mixing with seawater resulting in high salinity. Moreover, the drill stem test (DST) for CLB-1 well reports a salinity of 30,000 ppm for water samples from the Thebes reservoir. High porosity in both reservoirs is also indicated. High water saturation (SW) is a third important property characterizing the inferred geothermal reservoirs. The petrophysical parameters are summarized in Table 2 in supplementary file.

4.3. Fracture analysis and geomechanical modeling

4.3.1. Outcrop fracture analysis

The fault scarp of the HFF gave an opportunity for the complete analysis of fractures in the outcrop. This analysis is used to predict the fractures in the subsurface as well as geomechanical modeling. To facilitate data gathering, the fault scarp has been divided into four facets, numbered from first to fourth (Fig. 5 in supplementary file).

4.3.1.1. Fracture characterization. In each facet, the fracture characteristics were measured along scan lines. The fracture characteristics that were measured include fracture attitude (mainly strike orientation), spacing, average length, connectivity, and filling materials. Each facet is divided into fracture sets depending on their trends.

In the HF area, it is difficult to separate between background (regional) fractures and those related to the structuration in the area. This is because the area is affected elsewhere by normal faulting and the associated folds and fractures. The four studied facets are described below in detail. Field photos for each fracture facet as well as rose diagrams representing the orientation of the different fractures in each facet are given in Fig. 5 in supplementary file. The detailed fracture characteristics of each fracture set in each fracture facet are listed in Table 3 in supplementary file.

The first facet (to the northwest of the main hot spring site):

This facet consists of the white hard limestone of the Tanka Fm., the highly altered basaltic flow, and the mildly altered Thebes Fm. (Fig. 6a to 6d in supplementary file). The bedding of these rocks is dipping about 35° toward NW. Three dominant systematic fracture sets are observed along this facet including NW, NE, and WNW to ENE in a descending order of frequency (Fig. 5 in supplementary file). A less common NS oriented fracture set is also recorded.

The second facet (including the site of the main hot spring):

This facet seems to be the most important facet where the hot springs and the associated Thebes limestone host rock and the massive dolostones occur (Fig. 6f to 6h in supplementary file). This facet is characterized by high fracture density. The predominant fracture sets in this facet are the NW and NE-oriented fractures (Fig. 5 in supplementary file). The NE-oriented fractures have spacings that range between 2 and 3 m. The NW-oriented fractures have a moderate dip (40°- 60°) toward NE or SW. The NE-oriented fractures are nearly vertical to steeply dipping due to NW or SE. Non-systematic fractures are common and played a significant role in the connectivity between fractures of the different systematic fracture sets. Fracturing as well as brecciation, which were mentioned previously to be characteristic of the damage zone, are common in this facet.

The third facet (to the east of the main hot spring site):

This facet is dominated by the chalk of the Sudr Fm. The green to black shales of the Esna Fm. are also exposed at this facet (Fig. 6j to 6l in supplementary file). The fractures here are less dense than that of the second facet. This is attributed mainly to a lithological factor where the shale component of the facet a has lesser number of fractures. The fractures have the same orientation as the first and second facets with the same fracture sets. The order of the predominance of fracture orientations is NW then NE then WNW (Fig. 5 in supplementary file).

The fourth facet (to the east of the main hot spring site):

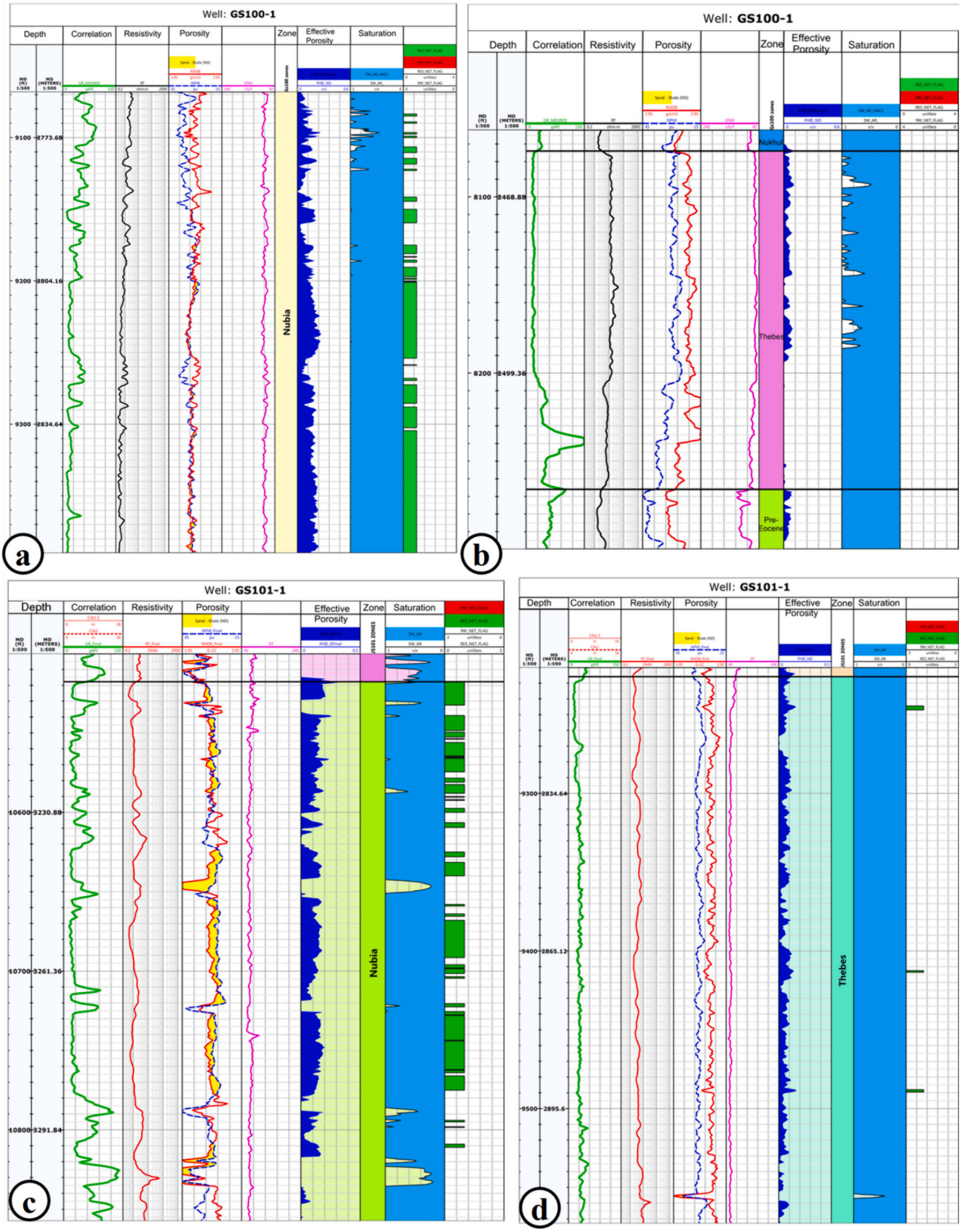

Fig. 3. Results of the petrophysical analysis of two offshore wells in the study area (GS 100–1 and GS 101–1 well). a & b) Computer-processed interpretation (CPI) plots of the Nubia zone and the Thebes zone of GS 100–1well respectively. c &d) CPI plots of the Nubia zone and the Thebes zone of GS 101–1well respectively combining the evaluated petrophysical parameters.

Table 2
the key variables used in Monte Carlo simulation for the prediction of the geothermal energy potential of HF area.

Reservoir		Reservoir Area (A) (km^2)	Reservoir Thickness (h) (m)	Reservoir Thickness (h) (km)	Reservoir Volume ($A{\cdot}h$) (km^3)	Reservoir Temperature (T_r) (°C)	Porosity (ϕ)	Recovery factor (R_f)
Nubia (onshore)	Min.	2.7	318.5	0.3185	0.85995	112	0.04	0.05
	Max.	8.16	432.9	0.4329	3.5324	142	0.264	0.33
	Most like	5.17	333.45	0.33345	1.7239	133	0.2	0.25
Nubia (offshore)	Min.	28	99.82	0.099	7.512	115	0.04	0.05
	Max.	115	256.6	0.2566	30.85	141	0.264	0.33
	Most like	99.37	106.5	0.1065	26.66	135	0.2	0.25
Thebes (offshore)	Min.	28	67.5	0.0675	1.35	94	0.024	0.03
	Max.	115	181	0.181	20.815	121	0.16	0.2
	Most like	99.37	102	0.102	28.28	115	0.15	0.1875

This facet is occupied by the Matulla Fm. (Fig. 6n in supplementary file). The younger units overlying the Matulla Fm. are not accessible. Fortunately, the fractures of the unreachable units are included in the other three facets. The fractures in the Matulla Fm. are short with a very narrow aperture. Although the fractures form a network, they are closed fractures with approximately zero communication. Conjugate fractures with NE orientation and small normal displacement are predominant in the lower part of the Matulla Formation. Fractures of random orientation are also common, where all of them are filled mainly with gypsum. The NW-oriented fracture set is the predominant one whereas the other sets are less common (Fig. 5 in supplementary file).

4.3.1.2. Origin of Fractures and factors controlling their distribution. The fractures in the study area are related mainly to normal faulting as well as fault-related folds associated with the GOS rift. Generally, the fractures associated with normal faulting are of two types; extension fractures and conjugate shear fractures (e.g., Fossen, 2010; Fig. 7a in supplementary file. There are two factors controlling their distribution: structural factor and lithological factor. The extension fractures are formed firstly in the history of the evolution of the normal fault with orientation nearly parallel to the strike of the fault. Later, the shear fractures are formed contemporaneously with the extension fractures and continue during the life of the normal fault. Furthermore, fracture sets may be found on fold structures (e.g., Stearns, 1969; Fig. 7b in supplementary file).

In the study area, the extension fractures have NW-SE strike and nearly vertical dip in the damage zone of HFF as well as GF 1. On the other hand, these fractures have NE strike around the GF 2. The conjugate shear fractures in the area are formed parallel to the strike of normal faults and dip about 60° away or toward their associated normal faults. The density of the extension fractures as well as the conjugate shear fractures decreases away from their normal faults (away from the damage zone). Moreover, the fractures associating the fault-related folds are mainly concentrated at the hinge zones of the rollover anticlines and fault propagation folds.

4.3.2. Geomechanical modeling

A geomechanical model (also known as a mechanical earth model or MEM) is a numerical depiction of the earth's rock properties, pore pressure (or fluid pressure), and stresses (e.g., Plumb et al., 2000). In other words, it is a data repository that records measurements of the mechanical characteristics of rocks and fractures, as well as the stresses and pressures acting on them at deep. This modeling technique is used to predict and understand the wellbore behavior to minimize drilling risks and improve well economics.

A MEM can capture a moment of interest, such as the virgin state of a reservoir, or it can monitor the changes that occur as the reservoir undergoes production (Last et al., 1995; Bérard and Prioul, 2016; Higgins-Borchardt et al., 2016). Understanding the current state of stress is the main component of an extensive geomechanical model. Knowledge of stress magnitude and orientations is of essential importance in addressing a wide range of geomechanical aspects within geothermal reservoirs and in overlying formations. These aspects include fracture initiation and propagation, permeability studies, and understanding of standing stress-generated hazards in the earth which is important for safe and effective drilling, reservoir evaluation, and development (Ali et al., 2003; Zoback, 2007; Ghassemi, 2012). It is also critical in the aspect of through-fractures fluid flow prediction since the stresses control which fractures are open and in what directions they propagate (Janis et al., 2016). Building a geomechanical model begins with the characterization of the reservoir and the overburden and then analyzing various types of data from available wells and other sources. These data include well logs, lithologic data, pressure, and stress measurements, as well as in-situ temperature. Mud logs, cutting data, and laboratory mechanical test data acquired from core samples are other sources. External databases, such as the World Stress Map, which is a worldwide collection of current tectonic stresses, can also be valuable in MEMs. The data are combined to produce different MEM components such as mechanical properties, pore pressure, and the magnitude and direction of the highest, intermediate, and minimum principal stresses. These elements are derived from direct observations, such as pore pressure and in situ stress testing, as well as indirect derivations based on rock physics modeling, such as pore pressure and principal stress models, as well as empirical correlations across datasets.

Pore pressure modeling takes into consideration the impacts of reservoir fluids that have accumulated over geologic time. Gravity, far-field tectonic stresses (remote stresses caused by tectonic plate movements), which are influenced by regional, basin, and local geologic structures, as well as by the current pore pressure are all taken into consideration in principal stress modeling. When available, calibration and validation of the MEM incorporate a variety of monitoring data such as drilling events and laboratory rock mechanical testing. (Ali et al., 2003; Baker Hughes, 2012; Bérard and Prioul, 2016; Janis et al., 2016).

Accordingly, a 1d geomechanical model of the HF geothermal system is built. This model relies on two main components; the first is the magnitudes of vertical stress or overburden stress, pore pressure, the maximum and minimum horizontal stresses. The second is the orientation of the minimum and maximum horizontal stresses. Constraining the stress magnitudes has been conducted using the well logs from the four used offshore wells (CLB-1, C2A-1, GS100–1, and GS101–1). The model is also calibrated by using MDT, Leak test, loss of circulation, and mud losses. The stress tensor has been concluded from focal mechanism revealed by the world stress map database (Heidbach et al., 2016). The goal is to understand the anisotropic permeability in fractured aquifers that results from the abundance and spread of faults and fractures, as well as the permeability related within the fault damage zone.

4.3.2.1. Vertical stress. The magnitude of vertical stress or the

overburden stress (S_v) can be calculated at any given depth (Z) by using the following equation:

$$S_v = \rho \cdot g \cdot Z \tag{10}$$

where the ρ is the density of overlying rock at depth Z and g is the acceleration due to gravity. By considering the water depth (Z_w) as in our case, the equation can be written as follow:

$$S_v = \rho \cdot g \cdot (Z - Z_w) \tag{11}$$

The density log is being used to compute the density of the overlying rock column. A problem is being faced where all the density logs are not being measured from the depth of zero. The Amoco extrapolation method is being used to overcome this problem. Density is being extrapolated up to the mud line using Amoco equation (Traugott, 1997):

$$\rho_{Amoco} = \rho_{mudline} + [(TVD - AG - Z_w)/3125]^{\alpha} \tag{12}$$

where ρ_{Amoco} is the extrapolated density in ppg (pounds per gallon), $\rho_{mudline}$ is the density at the mudline (seafloor) (default value is 16.3 ppg (1.95317 g/cm^3)), TVD is the true vertical depth, AG is the air gap, Z_w is the water depth and α is the exponent coefficient (default value is 0.6). All depths are in feet. Then, the two densities are combined, and the vertical stress has been calculated using the equation. The vertical stress gradients for the four wells are shown in Fig. 8 in supplementary file.

4.3.2.2. Hydrostatic and pore pressures. The pressure exerted per unit area by a column of water from sea level to a specific depth is referred to as hydrostatic (or normal) pressure. The following equation is used to compute this pressure:

$$P_{pnorm} = P_{po} + k \cdot TVD \tag{13}$$

where TVD is the true vertical depth, P_{po} is the pressure at the sea floor and k is a constant gradient equals to 0.44 psi/ft. (10 MPa/km)

After calculating the vertical stress (or overburden stress) from the density log, the pore pressure was also estimated from resistivity log and sonic log using resistivities of sediments and sonic compressional transit time, respectively by applying Eaton's method (Eaton, 1975):

$$P_p = S_v - (S_v - P_{pnorm}) \cdot (R_{Obs}/R_{norm})^n \tag{14}$$

$$P_p = S_v - (S_v - P_{pnorm}) \cdot (\Delta t_{norm}/\Delta t_{Obs})^n \tag{15}$$

where R_{Obs} is the resistivity obtained from well log (observed), R_{norm} is the resistivity at the normal (hydrostatic) pressure, Δt_{norm} is the sonic compressional transit time or slowness at the normal pressure conditions, Δt_{Obs} is the sonic transit time obtained (observed) from sonic log, and n is Eaton exponent which is normally equal to 1.2 for resistivity and equal to 3 for sonic.

The pore pressure is estimated (Fig. 9 in supplementary file) and calibrated with measured pressure points (MDT) and kick events which reflect abnormal pore pressure. The pore pressure curve gradients in the figure are those which were estimated from resistivity logs only as the resistivity curves were more continuous than sonic logs.

Generally, the pore pressure is hydrostatic, two over-pressurized zones are encountered at depths from 7500 ft. to 10,000 ft. (2286 m to 3048 m), and from 10,000 ft. to 12,500 ft. (3048 m to 3810 m) (Fig. 9 in supplementary file). These over-pressurized zones can be attributed to aqua thermal expansion. The concept of aqua thermal expansion was introduced by Barker (1972). Mouchet and Mitchell (1989) defined aquathermal expansion as the expansion of water due to thermal effects in a closed system. Mouchet and Mitchell (1989) concluded that this phenomenon requires a very well-sealed environment, with the temperature playing a chief role, and that it may be superimposed on the overburden effect. They reported also that the ideal environments for the aqua thermal expansion are closed systems with steep geothermal gradients and volcanic zones. Similarly, the volcanic activity in HF geothermal system seems to contribute to such phenomenon.

4.3.2.3. Horizontal stresses.

Stress tensor of the horizontal stresses:

Due to the lack of the four-arm caliper and FMI data, the current model relies on the World Stress Map project to predict the direction of horizontal stresses. The World Stress Map (WSM) (Heidbach et al., 2016) is a global collection of information on the crustal present-day stress field created by the Helmholtz Centre Potsdam - GFZ German Research Centre for Geosciences that has been updated since 2009. It is an academic-industry collaboration that strives to define the crustal stress pattern and identify the stress sources. The WSM revealed that the focal mechanism solutions nearby Hammam Faraun geothermal area are of the present-day normal faulting regime. The focal mechanism solutions are of A C-type data quality. Data on wellbore breakouts and drilling-induced fractures (Bosworth and Durocher, 2017) are also used to support the WSM data. It can be revealed that the orientation of maximum horizontal stress (S_{Hmax}) is NE-SW with $\pm 11^{\circ}$ deviation while the minimum horizontal stress (S_{hmin}) has an NW-SE orientation (Fig. 10 in supplementary file).

Minimum horizontal stress magnitude:

The magnitude of the minimum horizontal stress is estimated by the Mohr-Coulomb stress model (Zoback, 2007). The model is a failure model provides a relationship between two principal stresses if the formation is at failure. The algorithm which is being used is:

$$S_{hmin} = (S_v - \alpha \cdot P_p)/tan^2(\pi/4 + \varphi/2) + \alpha \cdot P_p \tag{16}$$

The main inputs for this algorithm are the vertical stress (S_v), the pore pressure (P_p), and the friction angle (φ), and α is the Biot coefficient which is usually close to 1. The friction angle is estimated from the gamma ray log.

The minimum horizontal stress is estimated (Fig. 11 in supplementary file) and calibrated by the leak-off test data found in the well logs, the complete loss of circulating mud, and finally the severe mud losses that are found in the well data (loss of circulation).

Maximum horizontal stress magnitude:

The most challenging stress tensor to evaluate is the maximum horizontal stress magnitude. The frictional faulting theory is a common method used in the estimation of the upper and lower boundaries of S_{Hmax}. Friction determines the limiting stress magnitudes as well as the direction of the faults that are prone to slip. Thus, probable stress conditions at any crustal depth may be defined providing that in-situ stress magnitudes in the crust do not exceed the criterion for frictional sliding on well-oriented faults (Peška and Zoback, 1995; Jaeger et al., 2007). Some appropriate boundary conditions have to be specified to reflect the range of possible stress states in the faulty compartment in order to depict the stress conditions for faulted reservoir systems under a wide variety of stress states. Consequently, the frictional strength of 'well orientated' pre-existing faults controls the maximum stress differential in a large volume of rock. The various values of S_{Hmax} and S_{hmin} may be simply represented as a polygonal-shaped area (Moos and Zoback, 1990; Peška and Zoback, 1995) that determines the stresses permissible by frictional strength of the crust at any given depth. It is a plot of S_{Hmax} versus S_{hmin} constrained by the strength of well-oriented, pre-existing faults. Stress states in which the crust is in frictional equilibrium correspond to points located on the tectonic regime polygon's periphery. These states can be classified as extensional stress (normal faulting), compressional stress (reverse faulting), or strike slip stress states.

According to Andersson's theory of faulting, in areas where

extensional forces dominate, the main horizontal stresses (S_{Hmax} and S_{hmin}) can be much smaller than the vertical stress (S_v). As a result, the directions of the intermediate stress (S_2 *or* σ_2) and the minimum stress (S_3 *or* σ_3) are horizontal, while the maximum stress (S_1 *or* σ_1) is vertical. On the other hand, in highly compressional areas, the opposite is observed, with the maximum (S_1*or* σ_1) and intermediate (S_2 *or* σ_2) stresses being horizontal, and the minimum stress (S_3 *or* σ_3) being vertical (Anderson, 1905).

The values of S_{hmin} and S_v at three different depths; 10,986 ft. (3348.533 m), 11,236 ft. (3424.733 m), and 11,536 ft. (3516.173 m) are acquired from Section 4.3.2.3 and extrapolated at the stress polygon (Fig. 12 in supplementary file). Consequently, the upper and the lower bounds of S_{Hmax} are drawn. The lower bound lies in the normal faulting regime zone (NF) while the upper bound lies in the strike-slip faulting regime zone (SS). As the HF area has mainly a normal faulting regime, the lower bound is chosen.

4.3.2.4. The final geomechanical model. The different gradients of the stress components and the pore pressure from the previous results are integrated to build the final 1D geomechanical model for the studied wells (Fig. 4).

4.3.3. Dilation tendency and geothermal significance

Ferrill et al. (1999) were the first to introduce the concept of dilation tendency. They explained it as the ability of a fracture to widen (dilate) and hence serve as a possible conduit for fluid movement. The resolved normal stress, which is a function of lithostatic and tectonic forces as well as fluid pressure, is primarily responsible for fracture dilation.

A fracture's aperture controls its ability to transmit fluids, the fracture's aperture is in turn related to effective normal stress acting on it. The normal stress experienced by a fracture is influenced by the magnitude and orientation of the principal stresses in relation to the fracture plane. The normal stress value can be calculated for surfaces of various orientations in a stress field that is known or hypothesized.

The dilation tendency (T_d) for the fractures has been calculated from the following equation (Ferrill et al., 1999):

$$T_d = (\sigma_1 - \sigma_n)/(\sigma_1 - \sigma_3) \quad (17)$$

where σ_1 is the maximum principal compressive stress, σ_3 is the minimum principal compressive stress, and σ_n is the normal stress.

The results were plotted on the Mohr-Coulomb circle (Fig. 13 in supplementary file). From the plots it can be concluded that the NE-SW

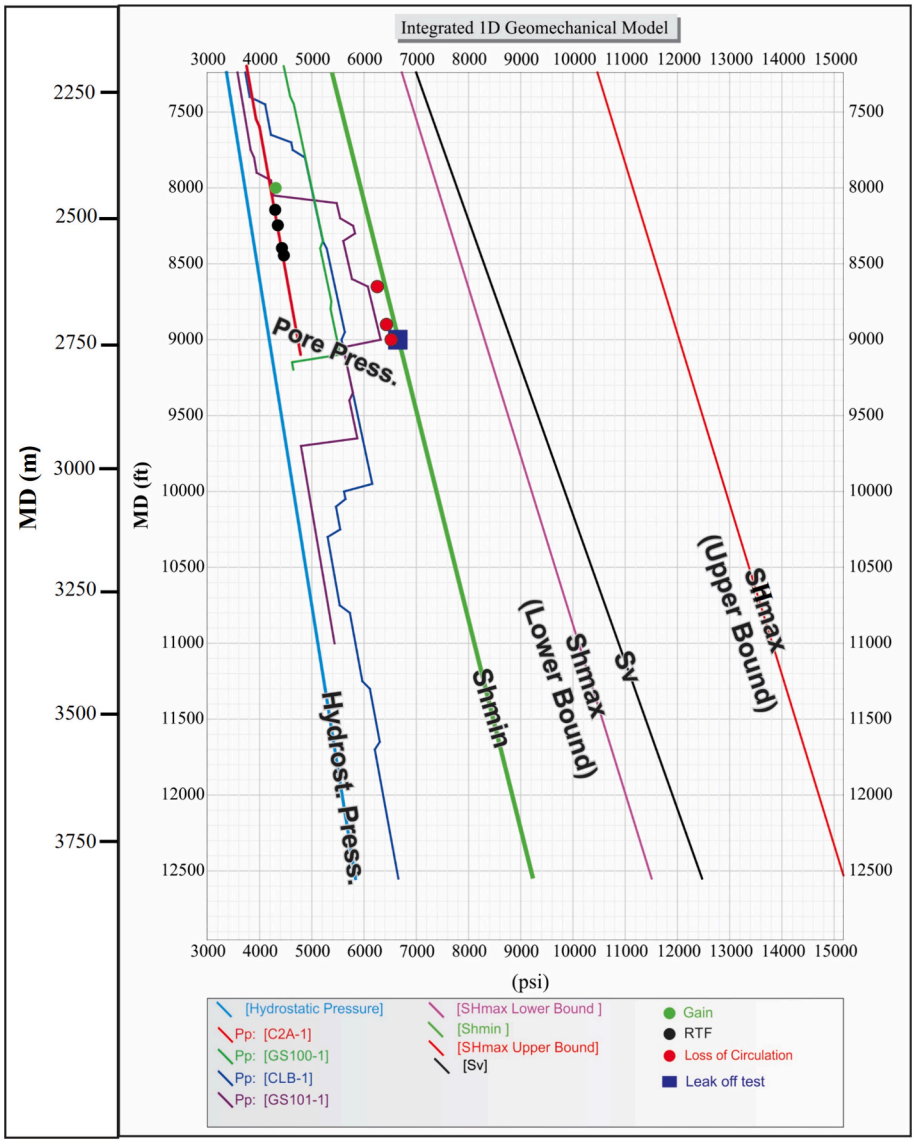

Fig. 4. Integrated 1d geomechanical model for the study area showing the different profiles (Depth in ft. vs stress in psi) for the vertical stress, minimum horizontal stress (S_{hmin}), and maximum horizontal stress (S_{Hmax}), alongside with hydrostatic and pore pressure.

fractures have the highest tendency to tensile failure when reaching the failure envelope. In other words, NE-SW-oriented fractures have higher dilation tendencies and thus are more likely to dilate than NW-SE fractures. These fractures are more concentrated in the breached HF relay ramp as mentioned previously. The required amount of pore pressure to reach the failure envelope is about 11.2 MPa. This value of pore pressure can be easily reached through the phenomenon of aqua thermal expansion of the hot water revealed from the over-pressurized zones noticed on the pore pressure gradient. In this respect, fracture dilation is primarily influenced by the resolved normal stress, which is determined by a combination of lithostatic and tectonic stresses, as well as fluid (hot water) pressure.

4.4. Volcanic activity and its geothermal significance

The results of the chemical analysis of the volcanic samples collected from the study area have been integrated with the results of Shallaly et al. (2013) and tabulated (Table 4 in supplementary file) to determine the degree of hydrothermal alteration of the Hammam Farun basaltic rocks compared to the nearby less altered rocks, and also to deduce crustal thickness.

4.4.1. Geochemistry

The HF fresh basalts have an average composition of 47.8 wt% SiO_2, 2.7 wt% TiO_2, 14.4 wt% Al_2O_3, 12.5 wt% Fe_2O_3, 5.5 wt% MgO, 10.6 wt % CaO, 2.5 wt% Na_2O, and 3.2 wt% P_2O_5. The altered basalts have a composition of 43.1 wt% SiO_2, 2.8 wt% TiO_2, and 15.8 wt% Al_2O_3, 11.6 wt% Fe_2O_3, 0.83 wt% MgO, 4.1 wt% CaO, 2.9 wt% Na_2O, 0.39 wt% P_2O_5. Comparing these average concentrations to those of Shallaly et al. (2013), it is obvious that the Hammam Faraun volcanics are not different from their equivalent rocks exposed along the Wadi Nukhul-Wadi Matulla-Abu Zenima join. Moreover, it is apparent that hydrothermal alteration affecting the rocks causes positive or negative change for certain elements, a drastic decrease of MgO and CaO of samples HF4 and HF5 and less commonly SiO_2, MnO, Co, Ni, and Y is observed (Table 4 in supplementary file). Conversely, a pronounced increase of K_2O, P_2O_5, Ba, Sr, Cu, Zr, Hf, and La (Table 4 in supplementary file) is recorded.

4.4.2. Crustal thickness

Trace elements are sensitive to crustal thicknesses, especially for modern volcanic suits. Rb—Sr relation (Condie, 1973) is used here to predict the crustal thickness of the Hammam Faraun area and environment during the eruption of the studied volcanic rocks. This Rb—Sr diagram suggests a crustal thickness of 20-30 km (Fig. 14 in supplementary file). This means the presence of magma storage at a depth of about 20-30 km. This thickness is in accordance with geophysical evidence which recorded the presence of the Moho at a depth of around 20 km (Saleh et al., 2006), reflecting the rise of the upper mantle at this part of the African curst. Moreover, a geochemical and mineral chemistry study (Shallaly et al., 2013) revealed the presence of two magma storages at the base of the crust under the Gulf of Suez area, a deeper one at 25–30 Km and a shallower one at 15–20 km.

Irrespective of the nature of the melt from which the basaltic rocks evolved being the asthenospheric mantle or the lithospheric, its presence at this depth that matters. The presence of the melt at that depth increases the geothermal gradient and hence affects the whole geothermic system in the Gulf of Suez rift basin.

4.4.3. Role of basalt on the geothermal system

Wall rock alteration near geothermal systems depends on the chemistry of the hydrothermal fluids and temperature (e.g., Franklin et al., 2005; Hannington et al., 2005; Boden, 2016). The study of mineralogy and geochemistry of basaltic rocks in the study area with an emphasis on secondary minerals shed some light on the factors controlling the hydrothermal system in the Hammam Faraun area. Secondary minerals are accumulated in the form of vesicles and fracture fillings and alteration of glass and primary phases as well. As mentioned earlier, alteration of the basalts is accompanied by a decrease or increase of certain elements. The decrease of Mg and Si associated with increasing of Ti, Fe, and Al is probably due to the progressive alteration of olivine to smectite and iddingsite as reported by Smith et al. (1987). The decrease of Ca and Mn might reflect the alteration of pyroxene. The increase of K and Ba may account for the formation of celadonite in the vesicles and/or sericitization of glassy mesostasis. Moreover, Zr, Nb, and Hf are considered immobile elements during alteration (Humphris and Thompson, 1978), in the case of the studied altered rocks a distinctive increase of these elements is recorded, (Table 4 in supplementary file). This may result from the leaching/reprecipitation processes of these HFS elements (e.g., Pandarinath et al., 2008). This conclusion is supported by the existence of abundant smectite that might adsorbed Zr and Nb (Shawky et al., 2021).

Though basaltic magma is anhydrous, it might have contributed to the fluids in the area. As the heat dissipated from the magma affected the country rock as the Sudr chalk which led to dehydration and decarbonatization reactions (Sharp et al., 2010) and the blackening of some parts of the Esna shale (Shawky et al., 2021), these fluids may have circulated with the meteoric water which affected the Hammam Faraun geothermal system during rift process. The concentration of certain secondary minerals in basaltic rocks in the area is also important. For instance, the basalts in the northwestern sector are characterized by a higher percentage of chalcedony and calcite, whereas those of the southeastern sector have higher percentages of smectite and celadonite (Shawky et al., 2021). Such mineral association indicates a low-sulfidation alteration (Boden, 2016), this kind of alteration is produced as a result of near-neutral-pH and alkali-chloride composition of the fluids, which depends mainly on temperature rather than other physical and chemical factors as in the high sulfidation alteration. The model proposes circulation of meteoric water through deep-sated fractures and faults in the study area to be heated by basaltic storage then causing alteration of the volcanic rocks and formation of smectite, Mn-epidote, and celadonite at deeper depth (SE sector), and chalcedony and calcite at shallower depths (NW sector). Based on mineral stabilities (Henley and Ellis, 1983) the temperature of the former setting ranges from 150 to 200 °C whilst that of the latter is around 100 °C. As the fluids reach the surface hot spring travertine is formed (Boden, 2016); the existence of the travertine deposits reported for the first time by Shawky et al. (2021) in the northwest sector of the area supports such a model.

4.5. Reservoir temperatures and geothermal gradient

The careful analysis of available temperature data from the used wells as well as from the literature led to a better understanding of the geothermal regime in HF area.

The onshore area that represents the footwall of HFF shows a geothermal gradient (G.G) of 48 °C/km and estimated heat flow ranging from 96 to 115 mW/m^2. These values are indicated from a specially drilled shallow borehole (80 m in the Eocene limestone) drilled at 200 m from the hot springs area (Morgan et al., 1985; Boulos, 1990). However, our constructed temperature profiles for the offshore wells (Fig. 15 in supplementary file) show geothermal gradients ranging from 29.7 °C/km in CLB-1 well to 38.2 °C/km in GS 100–1 well. The estimated reservoir temperature in the onshore area is between 112 and 142 °C for the Nubian Sandstone, with an average of 133 °C. On the other hand, the estimated reservoir temperature of the Nubian Sandstone for the offshore part is between 115 °C and 141 °C. For the Thebes reservoir, the estimated temperature is between 94 °C and 121 °C in the offshore area. These temperature values are taken from the minimum and maximum corrected temperatures for both reservoirs in the four wells except for the onshore area where the temperature is calculated using the geothermal gradient (48 °C/km, Morgan et al., 1985). These results were used in the simulation process for assessing the energy potential as

described below. Basement uplift and shallow volcanic intrusions in the onshore part account for the higher gradient in the onshore part. However, the geothermal resource in the offshore area is considerably large. Harnessing this offshore resource could be achieved through drilling onshore inclined geothermal wells.

4.6. Final geothermal conceptual model

Integration of all the results of this study allowed for the construction of an integrated conceptual geothermal model for the Hammam Faraun geothermal system demonstrating the different elements of the system. These elements include the heat source, the geothermal reservoirs, and the pathway of geothermal fluids.

4.6.1. Heat source

The Precambrian basement rocks are not only the heat source of the present geothermal system as suggested by previous authors (e.g. Abdel Zaher et al., 2011b), but also the Tertiary basaltic volcanic activity. This is attributed to the presence of a magma source at a depth of about 15–25 km. The high concentration of the basaltic dykes, sills and flows within the pre-rift succession may indicate that the magma chamber of the upwelled asthenosphere is large enough to keep heat beneath the HF hot springs area. In other words, excess heat flow accompanying the *syn*-rift volcanic activity is considered as the main heat source of the geothermal system.

4.6.2. Geothermal reservoirs

The main geothermal reservoirs are the Eocene Thebes carbonates and the Paleozoic to early Cretaceous Nubian Sandstone, with uncorrected reservoir temperatures of approximately 100 °C and 120 °C, and corrected reservoir temperatures of 120 °C and 140 °C, respectively. Water saturation in both reservoirs is approaching 100 %, explaining why the drilled wells in the study area for oil production were dry wells.

4.6.3. Geothermal fluids pathways

The Fault-related open fracture system characterized by structural permeability anisotropy is shown as the main pathway of the geothermal fluids. The fault activity during Gulf of Suez rifting made the rift faults including Hammam Faraun Fault and CLB fault have a high degree of transmissibility which facilitated the circulation of sea water between these two faults through the geothermal reservoirs. The fault-related open fracture system indicated by dilation tendency analysis is shown as the main pathway of geothermal fluids nowadays. The occurrence of a breached relay ramp (HF relay ramp) allowed fluid expulsion as hot springs which may explain the existence of hot springs specifically in this area exclusively from others. Relay zones are regarded not just lateral communication pathways for fluid flow across sealing faults, but also conduits of vertical fluid flow in petroleum, groundwater, CO2 sequestration, and magma settings (Fossen and Rotevatn, 2016).

The produced geological model from Petrel software for the subsurface area (Fig. 5a) is integrated with the surface geology results to construct the geothermal conceptual model of the study area (Fig. 5b).

These conceptual geothermal models are critical tools for estimating resource potential, guiding well targeting, describing reservoirs, assisting decision-making, and encouraging collaboration in geothermal exploration and development. They could provide a complete understanding of the geological structure of the geothermal system, allowing for the efficient and sustainable use of this renewable energy resource.

4.7. Geothermal potentiality assessment

4.7.1. Volumetric analysis

Volumes are calculated for the subsurface area mapped by seismic data. The calculations about the two studied reservoirs, Nubia, and Thebes, utilizing the depth structural maps for both reservoirs (refer to Fig. 4 in supplementary file). The boundaries for the calculated volumes are determined by the hanging wall cutoff line of the HFF from the northeast and the boundaries of the seismic data from the northwest, southeast, and southwest. The parameters considered in the calculations include water saturation, net gross, and porosity (Table 5 in supplementary file). These parameters are derived from the results of petrophysical analysis and well logs.

For the Nubian reservoir, a water saturation of 100 % is assumed, along with an average net-to-gross ratio of 0.5 and an average porosity of 20 %. Similarly, for the Thebes reservoir, a water saturation of 100 % is assumed, with a net-to-gross ratio of 0.5 and an average porosity of 15 %. The Nubian Sandstone group comprises sandstones and shales, with an average ratio of 1:1. Additionally, within the Thebes limestone, where shales are absent and fractures enhance the porosity, water-bearing horizons account for 50 % of the total thickness. This accounts for the selection of a net-to-gross ratio of 0.5.

By inputting these parameter values into Petrel software, it is determined that the volume of hot water in the offshore portion of the Nubia reservoir is approximately 225,967,200,000 ft^3 (5.332 km^3) and it is about 149,836,350,000 ft^3 (4.242 km^3) for the Thebes reservoir in the offshore part (Table 5 in supplementary file). These volumes are pore volumes because they account for the real volume of fluids inside the reservoir. Net volumes (the portion of the reservoir that can contain fluids) and average porosities from the volumetric analysis are used below in numerical simulation for the assessment of the geothermal power potential. Calculation of the Nubian reservoir volume in the onshore part revealed an average reservoir volume of 1.72 km^3 (Table 5 in supplementary file).

4.7.2. Numerical simulation of power potential

The key variables that impact energy output in Monte Carlo simulation include reservoir area, reservoir thickness, reservoir volume (Net volume), reservoir temperature, porosity, recovery factor, thermal efficiency, capacity factor of the power plant and running period of the power plant (Eqs. (5) to (9)).

The parameters used for both the Nubian and Thebes reservoirs are detailed in Table 2. The determination of used temperature values involved considering the lowest corrected temperature as the minimum temperature across the four wells. Conversely, the highest corrected temperature was regarded as the maximum temperature, while the medium corrected temperature was identified as the most likely temperature.

Regarding the reservoir area, the maximum extent encompassed the entire region surrounding HF (i.e. the whole mapped basin), encompassing the geologic data that indicated an extension of the geothermal reservoirs within the basin. In contrast, the minimum area was limited to a narrow zone surrounding the hot springs. The most likely area was defined as the region within the basin that included both the hot springs and the wells under study. In the evaluation of reservoir thickness, the maximum values were determined based on the longest thicknesses of the geothermal reservoirs inferred from well logs. Conversely, the minimum values were derived from the shortest thicknesses identified in the same well logs. The most likely thicknesses, also inferred from the well logs, were considered to be the medium values.

The recovery factor is calculated to be equal to $1.25 \cdot \phi$ (Muffler and Cataldi, 1978) where ϕ is the porosity. The thermal efficiency is assumed to be 10 %, while the capacity factor is 95 %.

According to the Monte Carlo simulation, the predicted generated geothermal power output at Hammam Faraun demonstrates promising values. Over a span of 25 years, a geothermal power plant utilizing the Nubian reservoir in the onshore area could generate an average power output of 9.64 MWe. Harnessing the Thebes reservoir in the offshore area, the average power output could reach 21.38 MWe, while utilizing the Nubian reservoir in the offshore area could yield a power output of 43.76 MWe (Fig. 6).

These power outputs have the potential to provide electricity to approximately 12,000 households, 29,000 households, and 53,000

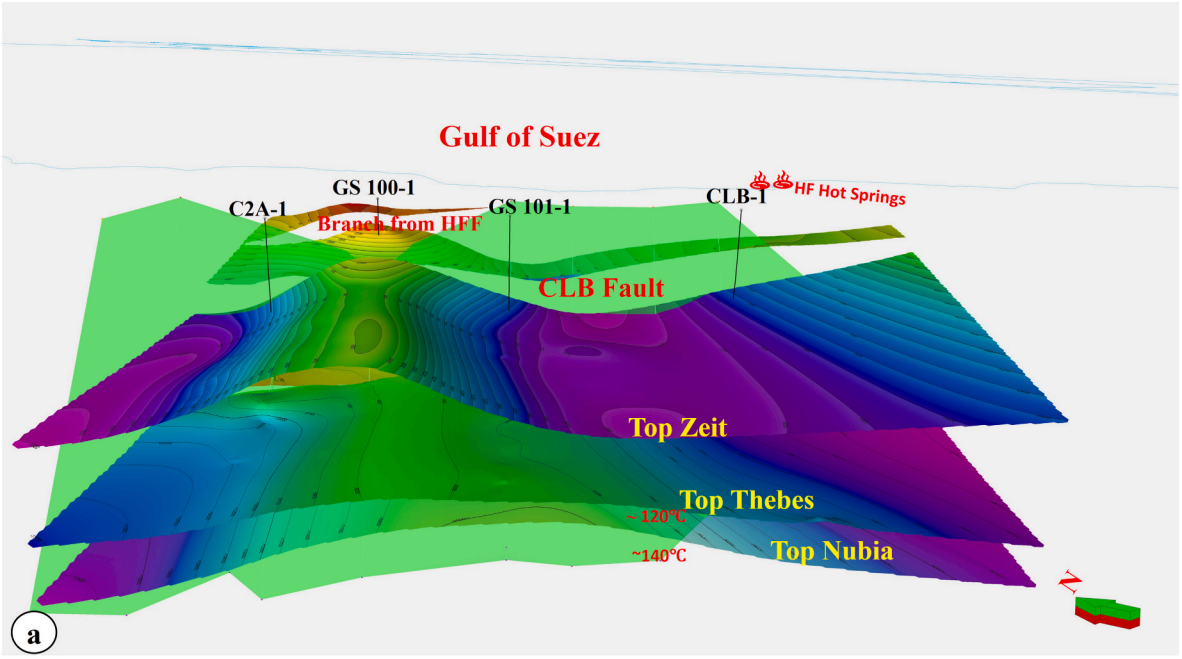

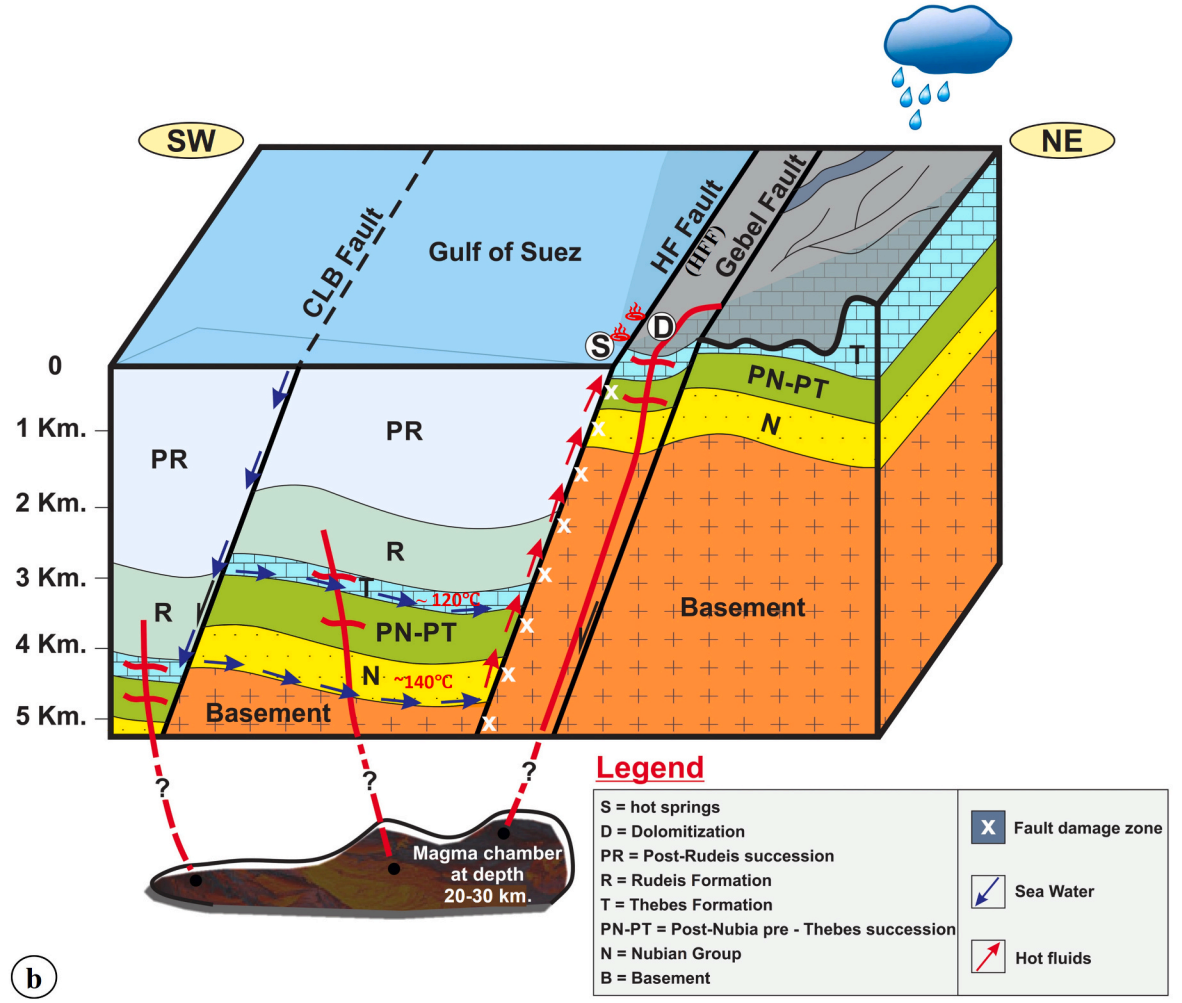

Fig. 5. a) 3D subsurface model for the offshore part of Hammam Faraun area, showing the different beds and structures. Only three main surfaces are shown (Zeit, Thebes, and Nubia). b) The final integrated conceptual model for Hammam Faraun geothermal system elaborating the different elements that contribute to the system.

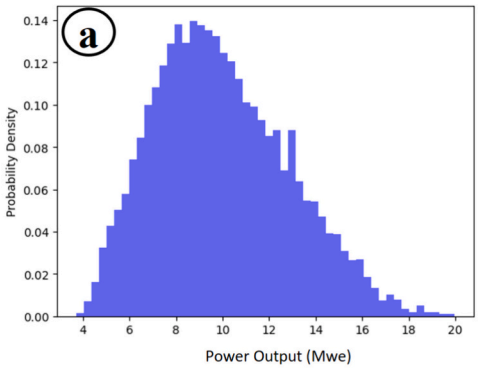

Nubia - Onshore (25 years):
Maximum Power Output: 19.98 MWe
Minimum Power Output: 3.70 MWe
Most Likely Power Output: 9.64 MWe

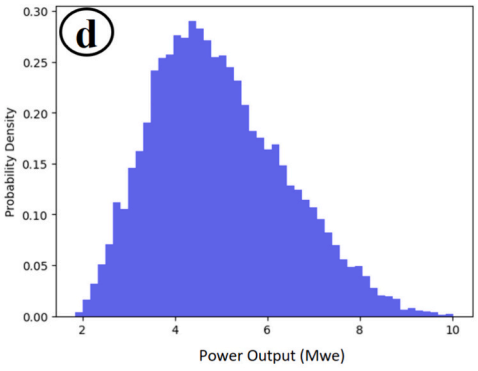

Nubia - Onshore (50 years):
Maximum Power Output: 10.03 MWe
Minimum Power Output: 1.83 MWe
Most Likely Power Output: 4.79 MWe

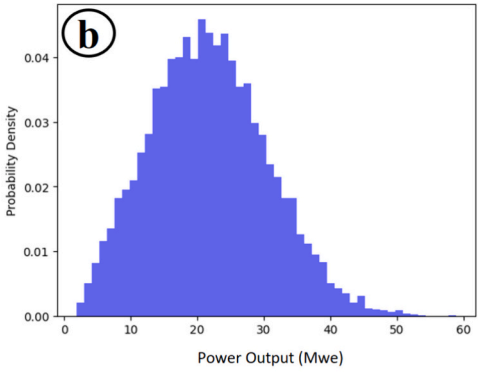

Thebes -Offshore (25 years):
Maximum power output 58.90 MWe
Minimum power output 1.83 MWe
Most likely power output 21.38 MWe

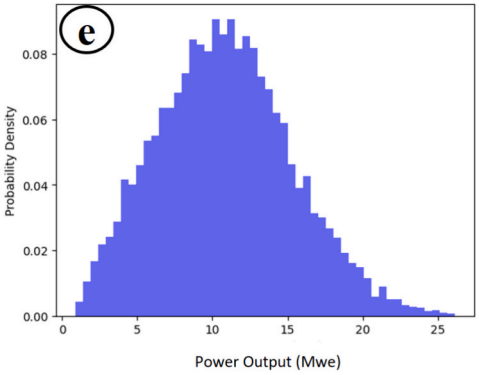

Thebes -Offshore (50 years):
Maximum power output 26.15 MWe
Minimum power output 0.87 MWe
Most likely power output 10.70 MWe

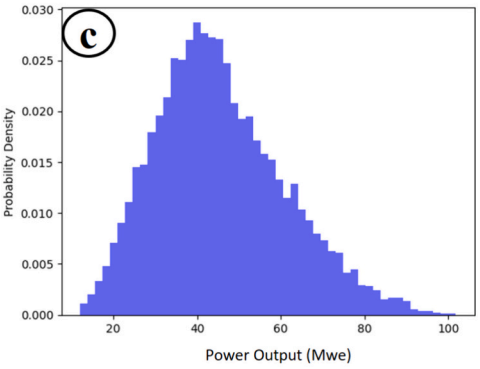

Nubia -Offshore (25 years):
Maximum Power Output: 101.81 MWe
Minimum Power Output: 12.06 MWe
Most Likely Power Output: 43.76 MWe

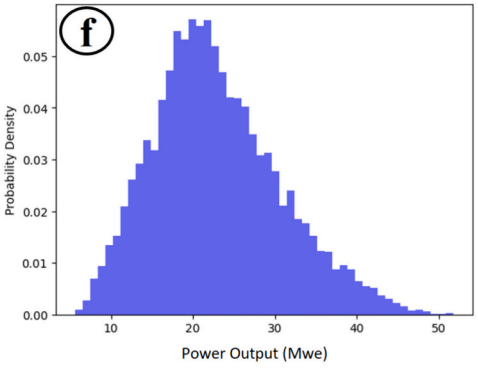

Nubia -Offshore (50 years):
Maximum Power Output: 51.80 MWe
Minimum Power Output: 5.59 MWe
Most Likely Power Output: 21.98 MWe

Fig. 6. Monte Carlo simulation results for the predicted generated geothermal power (Mwe) in HF area from both the Nubian reservoir and the Thebes reservoir for 25- years (a,b,c) and 50-years (d,e,f) scenarios.

households, respectively. These estimates are based on an assumed annual electricity consumption of 1700 kWh per capita (Enerdata, 2021), an average household size of 4 individuals (Africa Geoportal, 2023), and a power plant capacity factor of 95 % as mentioned previously. If the power plant operates for a lifespan of 50 years, approximately half of these power values and household numbers could be achieved (Fig. 6). The calculations here assume no heat recharge.

4.7.3. Resource type and potential uses

The geothermal resources of the Hammam Faraun area are classified here following the scheme of Hajto and Sowiżdżał (2018), which uses the most common and widely used temperature classification of geothermal systems according to Muffler and Cataldi (1978) and others (Table 6 in supplementary files). The geothermal resources are of the intermediate (or medium) enthalpy class.

Following the scheme of EGS (2020), and according to the estimated geothermal reservoir formation temperatures for the present geothermal

system (120–140 °C), it can be concluded that possible uses are a variety of direct uses as well as power generation using binary type power plant (Fig. 16 in supplementary file). This also comes from the knowledge that the hot springs occur at the surface and the depth to the geothermal reservoirs doesn't exceed about 3.5 Km in the offshore part. Direct uses need elevated but lower temperature fluids (generally 50 °C to 100 °C), which are primarily used in building heating (and sometimes cooling), but also for a variety of other purposes such as fish farming (aquaculture), fruit and vegetable drying, lumber processing, and, of course, bathing and soaking (e.g., Boden, 2016). Geothermal bathing is already applied in the area. Binary-cycle power plants are more complicated than other geothermal power plant types. The water they utilize is relatively low (<200 °C). The hot water in these power plants does not directly turn the turbine. Instead, when the water rises from a well, it passes through a heat exchanger. The heat exchanger transfers geothermal heat to a fluid with a lower boiling point. This second fluid then evaporates, turning the turbine (Wachtel, 2010). The working fluid in kalina-type binary plants is an ammonia-water mixture. We considered a temperature decrease of 20 °C for the geothermal fluid in the binary cycle heat exchanger at NH_3/H_2O high mass concentration of 90 %. The Kalina cycle improves turbine efficiency for geothermal fluids with lower temperatures (Boden, 2016). In agreement with Lashin (2013), Kalina power plants (Fig. 7) can be the most suitable geothermal power plant for power generation in Hammam Faraun area.

5. Conclusions

Subsurface geological analysis utilizing well-log data from abandoned wells, integrated with surface geology, led to producing a complete picture of Hammam Faraun geothermal system. Seismic interpretation, petrophysical investigation, fracture analysis, geochemical modeling, and BHT corrections, along with surface geochemical analysis, collectively contributed to the development of the final conceptual geothermal model. The presence of clysmic faults in the HF area establishes a renewable geothermal cycle, wherein seawater combines with formation waters that are heated by a magma source below. Geothermal fluids are discharged through the intersection of faults within a relay ramp zone. Geomechanical modeling enhanced the understanding of the geothermal fluids flow that is greatly linked to the fault- fractures system in the study area and this system explains why the hot springs continue to be recharged. High dilation tendencies of fractures and aquathermal expansion phenomenon inside the geothermal reservoir are the key factors to explain the flow of such geothermal fluids. The values of geothermal reservoir volumes together with the estimated reservoir temperatures (~120 °C and 140 °C), and the depth to reservoirs point to a medium enthalpy resource that is suitable for a variety of geothermal direct uses and indirect use (electricity generation) using a binary power plant of Kalina type. The predicted geothermal power values in HF area over a long period of years (25 years/50 years) using Monte Carlo simulation, are very encouraging (9.64 MWe to up to 43.76 MWe) and can serve the local populations in Sinai through providing clean electricity to a considerable number of households (12,000 up to 53,000 households). This work is a case study for a geothermal energy system in a rift basin that serves as a concise guiding model for further studies on geothermal systems in pervasive similar rift basin settings especially when associated with volcanic activity.

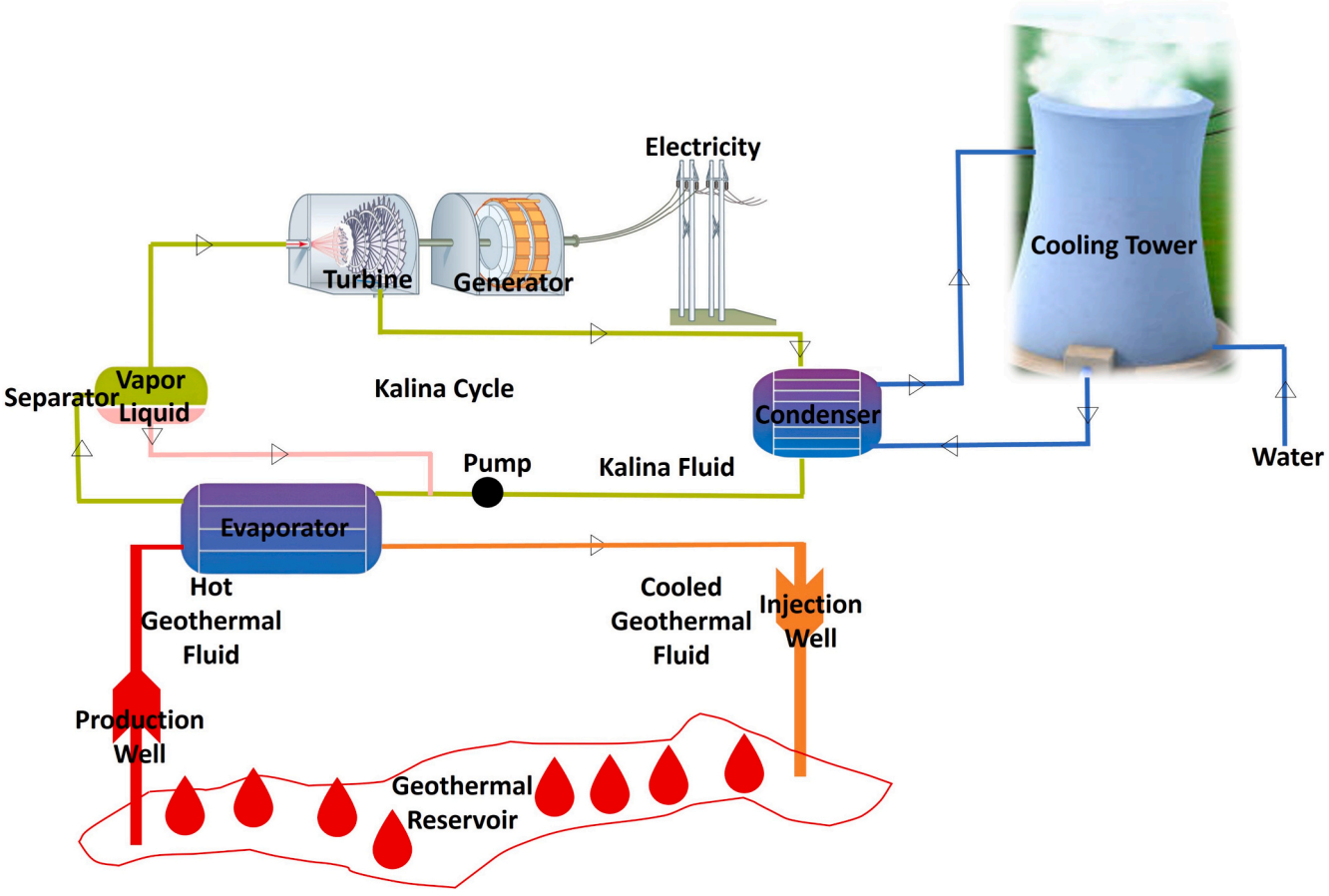

Fig. 7. An illustration for the proposed Kalina-type geothermal power plant for power production in Hammam Faraun area (based on Boghossian, 2011 and Kaczmarczyk et al., 2020).

CRediT authorship contribution statement

Ahmed Shawky: Writing – original draft, Visualization, Software, Methodology, Data curation, Conceptualization. **Mohamed Ibrahim El-Anbaawy:** Writing – review & editing, Supervision. **Reham Soliman:** Software. **Eslam Nasr Shaheen:** Software. **Osama Abdelaziz Osman:** Software. **Hesham Eid Abdel Hafiez:** Writing – review & editing, Supervision. **Nahla Ahmed Shallaly:** Writing – review & editing, Supervision.

Declaration of competing interest

Ahmed Shawky reports administrative support was provided by Cairo University. If there are other authors, they declare that they have no known competing financial interests or personal relationships that could have appeared to influence the work reported in this paper.

Data availability

The data that has been used is confidential.

Acknowledgments

The authors would like to acknowledge the Egyptian General Petroleum Corporation (EGPC) and the Gulf of Suez Petroleum Company (GUPCO) for providing the raw subsurface data used in this study and for granting permission to publish this work. Additionally, they wish to thank Schlumberger for providing academic licenses for the Petrel and Techlog software used in data interpretation and geomodelling (license no: 3-3797384; provided to the Geoinformatics lab of the Geology Department at Cairo University). Special thanks go to Prof. César Chamorro and Prof. Javier Rey (University of Valladolid) for their assistance during the second revision of the manuscript. Finally, the authors would like to extend their deep appreciation to Prof. Shawky Sakran (Cairo University) for his invaluable assistance and insightful discussions throughout this work.

Appendix A. Supplementary data

Supplementary data to this article can be found online at https://doi.org/10.1016/j.scitotenv.2024.174283.

References

Abdel Kader, Z., El Aref, M.M., 1986. On the formation of skarn rocks at Hammam Faraun. West Sinai, Egypt. J. Geol. 30, 89–108.

Abdel Zaher, M., El Nouby, M., Ghamry, E., Ehara, S., 2010. Contribution of geophysical and temperature logs data to geothermal exploration on the Gulf of Suez in Egypt. Proceedings of the World Geothermal Congress, Bali, Indonesia (pp. 25–29). http://www.geothermal-energy.org/pdf/IGAstandard/WGC/2010/1125.pdf.

Abdel Zaher, M., Ehara, S., El-Qady, G., 2011a. Conceptual model and numerical simulation of the hydrothermal system in Hammam Faraun hot spring, Sinai peninsula. Egypt. Arab. J. Geosci. 4, 161–170. https://doi.org/10.1007/s12517-009-0109-2.

Abdel Zaher, M., Nishijima, J., El-Qady, G., Aboud, E., Masoud, O., Soliman, M., Ehara, S., 2011b. Gravity and magnetotelluric investigations to elicit the origin of Hammam Faraun hot spring, Sinai peninsula. Egypt. Acta Geophys. 59, 633–656. https://doi.org/10.2478/s11600-011-0006-4.

Abdel Zaher, M.A., Saibi, H., Nishijima, J., Fujimitsu, Y., Mesbah, H., Ehara, S., 2012. Exploration and assessment of the geothermal resources in the Hammam Faraun hot spring, Sinai peninsula. Egypt. J. Asian Earth Sci. 45, 256–267. https://doi.org/10.1016/j.jseaes.2011.11.007.

Africa Geoportal, 2023. Average Household Size in Egypt. Retrieved October 6, 2023, from: https://www.africageoportal.com/maps/esri::average-household-size-in-egypt/about.

Ali, A.H.A., Brown, T., Delgado, R., Lee, D., Plumb, D., Smirnov, N., Marsden, R., Prado-Velarde, E., Ramsey, L., Spooner, D., Stone, T., 2003. Watching rocks change-mechanical earth modeling. Schlumberger Oilfield Review 15 (1), 22–39.

Alsharhan, A.S., 2003. Petroleum geology and potential hydrocarbon plays in the Gulf of Suez rift basin. Egypt. AAPG Bulletin 87 (1), 143–180. https://doi.org/10.1306/062002870143.

Anderson, E.M., 1905. The dynamics of faulting. Trans. Edinburgh Geol. Soc. 8 (3), 387–402. https://doi.org/10.1144/transed.8.3.387.

Atya, M.A., Khachay, O.A., Abdel Latif, A., Khachay, O.Y., El-Qady, G.M., Taha, A.I., 2010. Geophysical contribution to evaluate the hydrothermal potentiality in Egypt: case study: Hammam Faraun and Abu Swiera, Sinai. Egypt. Earth Sci. Res. J. 14 (1), 44–62.

Baker Hughes, 2012. Geomechanical Modeling Reduce risks across the life cycle of your assets.

Barker, C., 1972. Aquathermal pressuring–role of temperature in development of abnormal-pressure zones. AAPG Bull. 56 (10), 2068–2071. https://doi.org/10.1306/819A41B0-16C5-11D7-8645000102C1865D.

Barton, C.A., Zoback, M.D., Moos, D., 1995. Fluid flow along potentially active faults in crystalline rock. Geology 23, 683686. https://doi.org/10.1130/0091-7613(1995)023<0683:FFAPAF>2.3.CO;2.

Bérard, T., Prioul, R., 2016. Mechanical Earth Model. Schlumberger Oilfield Review, The Defining Series. https://www.slb.com/-/media/files/oilfield-review/defining-mem.ashx.

Boden, D.R., 2016. Geologic Fundamentals of Geothermal Energy, 1st ed. CRC Press. https://doi.org/10.1201/9781315371436. 425 p.

Boghossian, J.G., 2011. Dual-Temperature Kalina Cycle for Geothermal-Solar Hybrid Power Systems (Thesis (S.B.)). Massachusetts Institute of Technology, Dept. of Mechanical Engineering.

Bosworth, W., Durocher, S., 2017. Present-day stress fields of the Gulf of Suez (Egypt) based on exploratory well data: non-uniform regional extension and its relation to inherited structures and local plate motion. J. Afr. Earth Sci. 136, 136–147. https://doi.org/10.1016/j.jafrearsci.2017.04.025.

Boulos, F., 1989. Geothermal Development of Hammam Faraun Hot Spring. Sinai-Egypt, In International conference on applications of solar and renewable energy.

Boulos, F.K., 1990. Some aspects of the geophysical regime of Egypt in relation to heat flow, groundwater and microearthquakes. In: Said, R. (Ed.), The Geology of Egypt. Routledge, pp. 61–89.

Clennell, B., Esteban, L., Ricard, L., Josh, M., Liu, J., Regenauer-Lieb, K., 2010. Petrophysical Methods for Characterization of Geothermal Reservoirs. In: Proceedings of Australian Geothermal Energy Conference. Adelaide, Australia, pp. 123–129. https://www.geothermalenergy.org/pdf/IGAstandard/AGEC/2010/Esteban_et_al_2010.pdf.

Condie, K.C., 1973. Archean magmatism and crustal thickening. Geol. Soc. Am. Bull. 84 (9), 2981–2992. https://doi.org/10.1130/0016-7606(1973)84%3C2981:AMACT%3E2.0.CO;2.

Eaton, B.A., 1975. The equation for geopressure prediction from well logs: Society of Petroleum Engineers. In 50th Annual Meeting, Paper (No. 5544). https://doi.org/10.2118/5544-MS.

EGS, 2020. Development, Environmental and Geothermal Services (EGS). Retrieved November 1, 2023 from: http://envgeo.com/services/development/.

Egypt Upstream Gateway (EUG), 2021. Academic Research. Retrieved from: https://eug.petroleum.gov.eg/dp/jsp/AcademicResearch.jsp.

El Ramly, M.F., 1969. (1969): recent review of investigations on the thermal and mineral springs in the UAR. XXIII Int. Geologic Congress 19, 201–213.

Elbarbary, S., Abdel Zaher, M., Saibi, H., et al., 2022. Geothermal renewable energy prospects of the African continent using GIS. Geotherm. Energy 10, 8. https://doi.org/10.1186/s40517-022-00219-1.

Elmasry, A., Mohallel, S.A., Madani, A., Saibi, H., Abdel Zaher, M., Nassar, T., 2023. Geothermal groundwater study and its energetic potential assessment in Abu Gharadig Basin, North Western Desert. Egypt. J. Afr. Earth Sci. 202, 104925 https://doi.org/10.1016/j.jafrearsci.2023.104925.

El-Qady, G., Ushijima, K., Ahmad, E.S., 2000. Delineation of a geothermal reservoir by 2d inversion of resistivity data at Hamam Faraun area, Sinai, Egypt. In: Proceedings of the World Geothermal Congress, Kyushu - Tohoku, Japan. (pp. 1103–1108). http://www.geothermal-energy.org/pdf/IGAstandard/WGC/2000/R0195.PDF.

Enerdata, 2021. Egypt - Energy Consumption – Introduction. Retrieved October 6, 2023, from: https://www.enerdata.net/user/login/?destination=/egypt-energy-consumption-introduction.html.

Fatona, P., 2011. Renewable energy use and energy efficiency - a critical tool for sustainable development, sustainable growth and applications. In: Majid Nayeripour, M., Kheshti, M. (Eds.), Renewable Energy Sources. InTech, pp. 49–60.

Faulkner, D.R., Jackson, C.A.L., Lunn, R.J., Schlische, R.W., Shipton, Z.K., Wibberley, C. A.J., Withjack, M.O., 2010. A review of recent developments concerning the structure, mechanics and fluid flow properties of fault zones. J. Struct. Geol. 32 (11), 15571575. https://doi.org/10.1016/j.jsg.2010.06.009.

Ferrill, D.A., Winterle, J., Wittmeyer, G., Sims, D., Colton, S., Armstrong, A., Morris, A.P., 1999. Stressed rock strains groundwater at Yucca Mountain. Nevada. GSA Today 9 (5), 1–8. https://rock.geosociety.org/gsatoday/archive/9/5/.

Fossen, H., 2010. Structural geology. Cambridge University Press, Cambridge, p. 463.

Fossen, H., Rotevatn, A., 2016. Fault linkage and relay structures in extensional settings-a review. Earth Sci. Rev. 154, 14–28. https://doi.org/10.1016/j.earscirev.2015.11.014.

Franklin, J.M., Gibson, H.L., Jonasson, I.R., Galley, A.G., 2005. Volcanogenic Massive Sulfide Deposits. Society of Economic Geologists, In One Hundredth Anniversary Volume. https://doi.org/10.5382/AV100.17.

Fridleifsson, I.B., 2001. Geothermal energy for the benefit of the people. Renew. Sust. Energ. Rev. 5 (3), 299–312.

Fridleifsson, I.B., 2013. Geothermal–prospective energy source for developing countries. Technika Poszukiwań Geologicznych 52 (1), 143–159.

Frolova, J., Ladygin, V., Rychagov, S., 2001. Geothermal reservoir study through petrophysical data. Geotherm. Resour. Council Trans. 25, 401–403.

Gawthorpe, R.L., Jackson, C.A.L., Young, M.J., Sharp, I.R., Moustafa, A.R., Leppard, C. W., 2003. Normal fault growth, displacement localisation and the evolution of normal fault populations: the Hammam Faraun fault block, Suez rift. Egypt. J. Struct. Geol. 25 (6), 883–895. https://doi.org/10.1016/s0191-8141(02)00088-3.

Ghassemi, A., 2012. A review of some rock mechanics issues in geothermal reservoir development. Geotech. Geol. Eng. 30, 647–664. https://doi.org/10.1007/s10706-012-9508-3.

Giambiagi, L., Álvarez, P., Spagnotto, S., Godoy, E., Lossada, A., Mescua, J., Barrionuevo, M., Suriano, J., 2019. Geomechanical model for a seismically active geothermal field: insights from the Tinguiririca volcanic-hydrothermal system. Geosci. Front. 10 (6), 2117–2133. https://doi.org/10.1016/j.gsf.2019.02.006.

Glassley, W.E., 2015. Geothermal Energy: Renewable Energy and the Environment, Second Edition (2nd ed.). CRC Press. https://doi.org/10.1201/b17521.

Goldstein, B., Hiriart, G., Bertani, R., Bromley, C., Gutiérrez-Negrín, L., Huenges, E., Muraoka, H., Ragnarsson, A., Tester, J., Zui, V., 2011. Geothermal Energy. In IPCC Special Report on Renewable Energy Sources and Climate Change Mitigation [Edenhofer, O., Pichs-Madruga, R., Sokona, Y., Seyboth, K., Matschoss, P., Kadner, S., Zwickel, T., Eickemeier, P., Hansen, G., Schlömer, S., von Stechow, C. (eds)], Cambridge University Press, Cambridge, United Kingdom and New York, NY, USA. https://www.ipcc.ch/site/assets/uploads/2018/03/Chapter-4-Geothermal-Energy-1.pdf.

Hajto, M., Sowiżdżał, A., 2018. A global assessment of geothermal resources. In: Geothermal Water Management. CRC Press, pp. 3–29. https://doi.org/10.1201/9781315734972-1.

Hannington, M.D., de Ronde, C.D., Petersen, S., 2005. Sea-Floor Tectonics and Submarine Hydrothermal Systems. Society of Economic Geologists, Littelton, Colorado, USA, pp. 111–141. https://doi.org/10.5382/AV100.06.

Heidbach, O., Rajabi, M., Reiter, K., Ziegler, M., Team, W.S.M., 2016. World Stress Map Database Release 2016, V. 1.1. Services, GFZ Data. https://doi.org/10.5880/WSM.2016.001.

Henley, R.W., Ellis, A.J., 1983. Geothermal systems ancient and modern: a geochemical review. Earth Sci. Rev. 19 (1), 1–50. https://doi.org/10.1016/0012-8252(83)90075-2.

Higgins-Borchardt, S., Sitchler, J., Bratton, T., 2016. Geomechanics for unconventional reservoirs. In: Unconventional Oil and Gas Resources Handbook. Gulf Professional Publishing, pp. 199–213.

Hirani, J., 2014. Diagenetic Evaluation of Fault/Fracture Related Dolomitisation, Cretaceous-Eocene, Hammam Faraun Fault Block, Gulf of Suez. Ph.D. thesis,. University of Manchester, Manchester, United Kingdom, 295 p.

Hirani, J., Bastesen, E., Boyce, A., Corlett, H., Gawthorpe, R., Hollis, C., John, C.M., Robertson, H., Rotevatn, A., Whitaker, F., 2018a. Controls on the formation of stratabound dolostone bodies, Hammam Faraun fault block. Gulf of Suez. Sedimentology 65 (6), 973–2002. https://doi.org/10.1111/sed.12454.

Hirani, J., Bastesen, E., Boyce, A., Corlett, H., Eker, A., Gawthorpe, R., Hollis, C., Korneva, I., Rotevatn, A., 2018b. Structural controls on non-fabric selective dolomitization within rift- related basin-bounding normal fault systems: insights from the Hammam Faraun fault, Gulf of Suez. Egypt. Basin Res. 30 (5), 990–1014. https://doi.org/10.1111/bre.12290.

Hollis, C., Bastesen, E., Boyce, A., Corlett, H., Gawthorpe, R., Hirani, J., Rotevatn, A., Whitaker, F., 2017. Fault-controlled dolomitization in a rift basin. Geology 45 (3), 219–222. https://doi.org/10.1130/G38s394.1.

Hubbert, M., Rubey, W.W., 1959. Role of fluid pressure in mechanics of overthrust faulting: I. Mechanics of fluid-filled porous solids and its application to overthrust faulting. Geol. Soc. Am. Bull. 70 (2), 115–166. https://doi.org/10.1130/0016-7606(1959)70[115:ROFPIM]2.0.CO;2.

Humphris, S.E., Thompson, G., 1978. Trace element mobility during hydrothermal alteration of oceanic basalts. Geochim. Cosmochim. Acta 42 (1), 127–136. https://doi.org/10.1016/0016-7037(78)90222-3.

IRENA, 2017. Geothermal Power: Technology Brief. International Renewable Energy Agency, Abu Dhabi. https://www.irena.org/publications/2017/Aug/Geothermal-power-Technology-brief.

Jackson, C.A., Gawthorpe, R.L., Leppard, C.W., Sharp, I.R., 2006. Rift-initiation development of normal fault blocks: insights from the Hammam Faraun fault block, Suez rift. Egypt. J. Geol. Soc. 163 (1), 165–183. https://doi.org/10.1144/0016-764904-164.

Jackson, C.A.L., Gawthorpe, R.L., Sharp, I.R., 2002. Growth and linkage of the east Tanka fault zone, Suez rift: structural style and syn-rift stratigraphic response. J. Geol. Soc. Lond. 159 (2), 175–187. https://doi.org/10.1144/0016-764901-100.

Jaeger, J.C., Cook, N.G.W., Zimmerman, R.W., 2007. Fundamentals of Rock Mechanics, 4th edn. Blackwell, Maiden, MA, p. 475.

Janis, M., Liu, J., Ghassemi, A., 2016. Reservoir geomechanics model for EGS. In: 40th GRC Annual Meeting, Sacramento, CA, USA, pp. 345–352.

Kaczmarczyk, M., Tomaszewska, B., Pająk, L., 2020. Geological and thermodynamic analysis of low enthalpy geothermal resources to electricity generation using ORC and Kalina cycle technology. Energies 13 (6), 1335. https://doi.org/10.3390/en13061335.

Kombe, E.Y., Muguthu, J., 2019. Geothermal energy development in East Africa: barriers and strategies. J. Energy Res. Rev. 2, 1–6.

Korneva, I., Bastesen, E., Corlett, H., Eker, A., Hirani, J., Hollis, C., Gawthorpe, R.L., Rotevatn, A., Taylor, R., 2018. The effects of dolomitization on petrophysical properties and fracture distribution within rift-related carbonates (Hammam Faraun fault block, Suez rift, Egypt). J. Struct. Geol. 108, 108–120. https://doi.org/10.1016/j.jsg.2017.06.005.

Lashin, A., 2013. A preliminary study on the potential of the geothermal resources around the Gulf of Suez. Egypt. Arab. J. Geosci. 6, 2807–2828. https://doi.org/10.1007/s12517-012-0543-4.

Last, N., Plumb, R., Harkness, R., Charlez, P., Alsen, J., McLean, M., 1995. An Integrated Approach to Evaluating and Managing Wellbore Instability in the Cusiana Field. In SPE annual technical conference and exhibition. OnePetro, Colombia, South America. https://doi.org/10.2118/30464-MS.

Magaritz, M., Issar, A., 1973. Carbon and oxygen isotopes in epigenetic hydrothermal rocks from Hamam-el-Farun. Sinai. Chem. Geol. 12 (2), 137–146. https://doi.org/10.1016/0009-2541(73)90111-3.

Moeck, I., Kwiatek, G., Zimmermann, G., 2009. Slip tendency analysis, fault reactivation potential and induced seismicity in a deep geothermal reservoir. J. Struct. Geol. 31 (10), 1174–1182. https://doi.org/10.1016/j.jsg.2009.06.012.

Moeck, I.S., 2014. Catalog of geothermal play types based on geologic controls. Renew. Sust. Energ. Rev. 37, 867–882. https://doi.org/10.1016/j.rser.2014.05.032.

Moos, D., Zoback, M.D., 1990. Utilization of observations of well bore failure to constrain the orientation and magnitude of crustal stresses: application to continental, Deep Sea drilling project, and ocean drilling program boreholes. J. Geophys. Res. Solid Earth 95 (B6), 9305–9325. https://doi.org/10.1029/jb095ib06p09305.

Morgan, P., Boulos, F.K., Hennin, S.F., El-Sherif, A.A., El-Sayed, A.A., Basta, N.Z., Melek, Y.S., 1985. Heat flow in eastern Egypt: the thermal signature of a continental breakup. J. Geodyn. 4 (1–4), 107–131. https://doi.org/10.1016/0264-3707(85)90055-9.

Morris, A., Ferrill, D.A., Henderson, D.B., 1996. Slip-tendency analysis and fault reactivation. Geology 24 (3), 275–278. https://doi.org/10.1130/00917613(1996)024%3C0275:STAAFR%3E2.3.CO;2.

Mouchet, J.P., Mitchell, A., 1989. Abnormal pressures while drilling: origins, prediction, detection, evaluation (Vol. 2). Editions Technip.

Moustafa, A.R., Abdeen, M.M., 1992. Structural setting of the Hammam Faraun block, eastern side of the Suez rift. J. Univ. Kuwait (Sci.) 19, 291–310.

Moustafa, A.R., Khalil, S.M., 2017. Control of extensional transfer zones on syntectonic and post-tectonic sedimentation: implications for hydrocarbon exploration. J. Geol. Soc. Lond. 174 (2), 318–335. https://doi.org/10.1144/jgs2015-138.

Muffler, P., Cataldi, R., 1978. Methods for regional assessment of geothermal resources. Geothermics 7 (2–4), 53–89. https://doi.org/10.1016/0375-6505(78)90002-0.

Oyedotun, T.D.T., 2018. X-ray fluorescence (XRF) in the investigation of the composition of earth materials: a review and an overview. Geol. Ecol. Landsc. 2 (2), 148–154. https://doi.org/10.1080/24749508.2018.1452459.

Pandarinath, K., Dulski, P., Torres-Alvarado, I.S., Verma, S.P., 2008. Element mobility during the hydrothermal alteration of rhyolitic rocks of the Los Azufres geothermal field. Mexico. Geothermics 37 (1), 53–72. https://doi.org/10.1016/j.geothermics.2007.10.002.

Peška, P., Zoback, M.D., 1995. Compressive and tensile failure of inclined well bores and determination of in situ stress and rock strength. J. Geophys. Res. Solid Earth 100 (B7), 12791–12811. https://doi.org/10.1029/95jb00319.

Petroleum Experts Limited, 2024. FieldMove Clino. Smartphone application available at: https://play.google.com/store/apps/details?id=com.mve.fieldmove.clino&hl=es_419.

Plumb, R., Edwards, S., Pidcock, G., Lee, D., Stacey, B., 2000. The mechanical earth model concept and its application to high-risk well construction projects. In: SPE/IADC Drilling Conference and Exhibition. SPE. https://doi.org/10.2118/59128-MS (pp. SPE-59128).

Pocasangre, C., Fujimitsu, Y., 2018. A Python-based stochastic library for assessing geothermal power potential using the volumetric method in a liquid-dominated reservoir. Geothermics 76, 164–176. https://doi.org/10.1016/j.geothermics.2018.07.009.

Rotevatn, A., Bastesen, E., 2014. Fault linkage and damage zone architecture in tight carbonate rocks in the Suez rift (Egypt): implications for permeability structure along segmented normal faults. Geol. Soc. Lond. Spec. Publ. 374 (1), 79–95. https://doi.org/10.1144/SP374.12.

Saleh, S., Jahr, T., Jentzsch, G., Saleh, A., Abou Ashour, N.M., 2006. Crustal evaluation of the northern Red Sea rift and Gulf of Suez, Egypt from geophysical data: 3-dimensional modeling. J. Afr. Earth Sci. 45 (3), 257–278. https://doi.org/10.1016/j.jafrearsci.2006.02.001.

Schumacher, S., Moeck, I., 2020. A new method for correcting temperature log profiles in low-enthalpy plays. Geotherm. Energy 8, 27. https://doi.org/10.1186/s40517-020-00181-w.

Shallaly, N.A., Beier, C., Haase, K.M., Hammed, M.S., 2013. Petrology and geochemistry of the tertiary Suez rift volcanism, Sinai. Egypt. J. Volcanol. Geotherm. Res. 267, 119–137. https://doi.org/10.1016/j.jvolgeores.2013.10.005.

Shallaly, N.A., Kabesh, M., Shawky, A., El-Anbaawy, M.I., Shaheen, E.N., 2023. Skarn and peperite formation within the frame of rifting dynamics, sedimentation, and magmatic activities, Hammam Faraun, Gulf of Suez. Egypt. J. Afr. Earth Sci. 199, 104853 https://doi.org/10.1016/j.jafrearsci.2023.104853.

Sharp, I., Gillespie, P., Morsalnezhad, D., Taberner, C., Karpuz, R., Vergés, J., Horbury, A., Pickard, N., Garland, J., Hunt, D., 2010. Stratigraphic architecture and fracture-controlled dolomitization of the cretaceous Khami and Bangestan groups: an outcrop case study, Zagros Mountains. Iran. Geological Society, London, Special Publications 329 (1), 343–396. https://doi.org/10.1144/SP329.14.

Sharp, I.R., Gawthorpe, R.L., Underhill, J.R., Gupta, S., 2000. Fault propagation folding in extensional settings: examples of structural style and synrift sedimentary response from the Suez rift, Sinai. Egypt. Geol. Soc. Am. Bull. 112, 1877–1899. https://doi.org/10.1130/0016-7606(2003)115%3C0640:FFIESE%3E2.0.CO;2.

Shawky, A., El-Anbaawy, M.I., Shallaly, N.A., Abdelhafiz, H.E., 2020. Geotouristic Potentiality Of Hammam Faraun Geothermal Area, South Sinai Governorate, Egypt. Egypt. J. Geol. 64, 189–204. https://doi.org/10.21608/egjg.2020.215757.

Shawky, A., El-Anbaawy, M.I., Shallaly, N.A., Abdelhafiz, H.E., Shaheen, E.N., 2021. Continuous fluid circulation in Hammam Faraun geothermal system, Gulf of Suez

rift, Egypt: evidences from hydrothermal deposits along rift-related faults. Carbonates Evaporites 36, 1–18. https://doi.org/10.1007/s13146-021-00721-w.
Sibson, R.H., 1977. Fault rocks and fault mechanisms. J. Geol. Soc. Lond. 133 (3), 191–213. https://doi.org/10.1144/gsjgs.133.3.0191.
Sibson, R.H., 1996. Structural permeability of fluid-driven fault-fracture meshes. J. Struct. Geol. 18 (8), 1031–1042. https://doi.org/10.1016/0191-8141(96)00032-6.
Siler, D.L., Faulds, J.E., Hinz, N.H., 2015. Earthquake-related stress concentrations and permeability generation in geothermal systems. GRC Transactions 39, 437–444. http://pubs.geothermal-library.org/lib/grc/1032180.pdf.
SLB (Schlumberger), 2024a. Petrel subsurface software. Retrieved from: https://www.software.slb.com/products/petrel.
SLB (Schlumberger), 2024b. Techlog wellbore software. Retrieved from: https://www.software.slb.com/products/techlog.
Smith, K.L., Milnes, A.R., Eggleton, R.A., 1987. Weathering of basalt: formation of iddingsite. Clay Clay Miner. 35 (6), 418–428. https://doi.org/10.1346/CCMN.1987.0350602.
Stearns, D.W., 1969. Fracture as a mechanism of flow in naturally deformed layered rocks. In proceedings of the conference on research in tectonics, kink bands and brittle deformation. Geol. Surv. Can. Pap. 68 (52), 79–96.
Steen, G., 1982. Radiometric age dating of some Gulf of Suez igneous rocks. Proceedings of the 6th Exploration Seminar. Egyptian General Petroleum cooperation and Egypt petroleum exploration society, Cairo, pp. 199–211.
Swanberg, C.A., Morgan, P., Boulos, F.K., 1983. Geothermal potential of Egypt. Tectonophysics 96 (1–2), 77–94. https://doi.org/10.1016/0040-1951(83)90245-7.
Tezuka, K., Niitsuma, H., 2000. Stress estimated using microseismic clusters and its relationship to the fracture system of the Hijiori hot dry rock reservoir. In: Developments in Geotechnical Engineering, vol. 84. Elsevier, pp. 55–70. https://doi.org/10.1016/S0165-1250(00)80007-3.
Townend, J., Zoback, M.D., 2000. How faulting keeps the crust strong. Geology 28 (5), 399–402. https://doi.org/10.1130/0091-7613(2000)28.
Traugott, M., 1997. Pore/fracture pressure determinations in deep water. World Oil 218 (8), 68–70. Suppl. August, 8 p.
Wachtel, A., 2010. Geothermal Energy. Chelsea Clubhouse, 48 p.
Waples, D.W., Pacheco, J., Vera, A., 2004. A method for correcting log-derived temperatures in deep wells, calibrated in the Gulf of Mexico. Pet. Geosci. 10 (3), 239–245. https://doi.org/10.1144/1354-079302-542.
ZetaWare, 2003. Utilities — BHT Correction. https://www.zetaware.com/utilities/bht/waples_gom.html.
Zoback, M.D., 2007. Reservoir Geomechanics. Cambridge University Press, 459 p.